

rf-induced heating dynamics of noncrystallized trapped ions

Martin W. van Mourik ¹, Pavel Hrmo ¹, Lukas Gerster ¹, Benjamin Wilhelm ¹, Rainer Blatt,^{1,2}
Philipp Schindler,¹ and Thomas Monz^{1,3}

¹*Institut für Experimentalphysik, Universität Innsbruck, Technikerstraße 25/4, 6020 Innsbruck, Austria*

²*Institut für Quantenoptik und Quanteninformation, Österreichische Akademie der Wissenschaften,
Technikerstraße 21a, 6020 Innsbruck, Austria*

³*AQT, Technikerstraße 17, 6020 Innsbruck, Austria*



(Received 18 May 2021; revised 8 November 2021; accepted 17 February 2022; published 7 March 2022)

We investigate the energy dynamics of noncrystallized (melted) ions, confined in a Paul trap. The nonperiodic Coulomb interaction experienced by melted ions forms a medium for nonconservative energy transfer from the radio-frequency (rf) field to the ions, a process known as rf heating. We study rf heating by analyzing numerical simulations of noncrystallized ion motion in Paul trap potentials, in which the energy of the ions' secular motion changes at discrete intervals, corresponding to ion-ion collisions. The analysis of these collisions is used as a basis to derive a simplified model of rf heating energy dynamics, from which we conclude that the rf heating rate is predominantly dependent on the rf field strength. We confirm the predictability of the model experimentally: Two trapped $^{40}\text{Ca}^+$ ions are deterministically driven to melt, and their fluorescence rate is used to infer the ions' energy. Under these experimental conditions, we investigate which Doppler cooling parameters are required for efficient recrystallization, and compare our results to simulations.

DOI: [10.1103/PhysRevA.105.033101](https://doi.org/10.1103/PhysRevA.105.033101)

I. INTRODUCTION

Ions confined in radio-frequency (rf) Paul traps have enabled research in many fields of physics [1], such as fundamental light-matter interactions [2,3], frequency measurements and metrology [4], mass spectrometry [5], quantum computation [6–9], and quantum simulation [10–12]. The vast majority of modern trapped-ion experiments utilize a so-called ion crystal, a regular spatial structure of multiple ions. Such experiments rely on the fact that these crystals contain well-localized separated particles that share common motional modes due to their Coulomb interaction. For example, in trapped-ion-based quantum computation, an ion crystal represents a qubit register, and their common motional modes are the data bus that mediates entanglement [13,14].

A prominent event that disturbs the crystal structure is a collision with a particle from the residual background gas [15]. Such a collision can transfer enough energy to the ions such that the crystal structure is destroyed. The ions undergo a transition described as melting, to a phase colloquially named an ion cloud [16,17], and are no longer suitable to be used as qubits for quantum computation.

Melted ions are subjected to a change in energy that is not present in the crystal phase: Energy can be transferred to the ions from the rf field from the trapping electrodes, leading to an overall increase in the ions' average kinetic energy. This process, known as *rf heating*, occurs when ions experience both nonperiodic Coulomb forces and forces from the trap's oscillating rf field. rf heating has previously been studied in the context of interactions of ions with ultracold buffer gases [18,19] and ion ensembles [20–23].

The performance of trapped-ion experiments benefits from efficiently returning an ion cloud into the crystal state, a process known as *recrystallization*. While laser-cooling techniques can be employed to remove energy from the ions, the opposing increase in energy due to rf heating hinders or even prevents recrystallization.

rf heating due to ion-ion interactions is a dominant source of energy gain in ion clouds, even for low numbers of ions. Despite melting being a common occurrence in ion trap experiments, rf heating has not been studied in detail, even for the simplest case: two trapped ions. In fact, rf heating is often mistakenly dismissed as playing only a minor role in melted ion dynamics. Consequently, it has not previously been investigated which laser cooling conditions are necessary to ensure efficient recrystallization.

In this work, we study the dynamics of rf heating in ion clouds. We aim to improve the general understanding of rf heating by introducing an intuitive overview of the processes involved, and providing relevant magnitudes and timescales of energy changes. As the motion of melted ions in an rf field is chaotic [17,24,25], it is inconceivable to attain generalized analytic descriptions of the ion motion [20]. However, we can numerically analyze dynamics of melted ions with multiple initial conditions, from which we derive simplified models that provide quantitative approximations of the effects of rf heating. This approach allows us to estimate the cooling rates that are required for overcoming rf heating. We experimentally investigate rf heating of a two-ion single-species ion cloud, and determine which Doppler cooling parameters are required to recrystallize it efficiently. The experimental results are

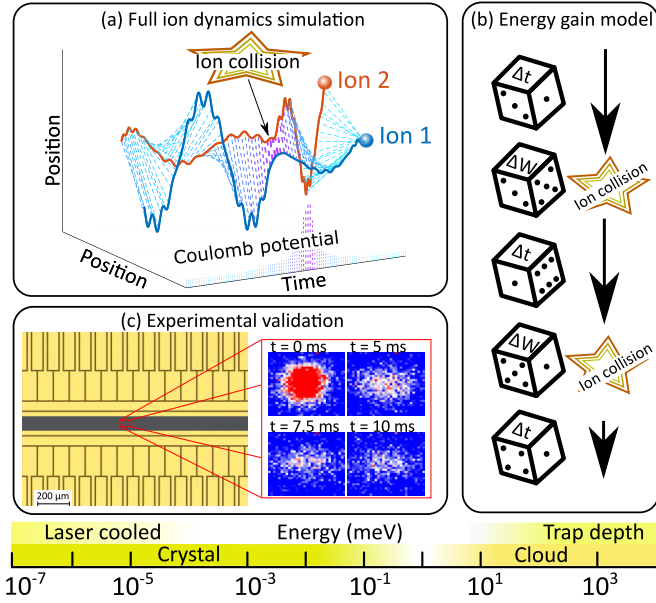


FIG. 1. Schematic outline: (a) We simulate the full three-dimensional (3D) dynamics of ions in a time-dependent field allowing us to numerically analyze the processes that lead to energy change. (b) Our analysis is used as a basis for a simplified model that describes the rf heating rate. (c) We experimentally create controlled melting events, from which we estimate the ion cloud energy. For reference, typical energy scales are displayed for relevant regimes.

compared to heating and cooling dynamics that are predicted by our model.

This paper is structured as follows. In Sec. II we provide a general description of the process of rf heating. Subsequent sections (III–V) detail our investigation of rf heating in three steps, as schematically depicted in Figs. 1(a)–1(c). In Sec. III, we use numerical simulations that track the motion of ions in a Paul trap to investigate their dynamics under the influence of an rf field and Coulomb interaction. From these simulations we surmise that changes in energy due to rf heating occur at discrete moments in time, corresponding to small ion-ion distances that lead to a large Coulomb repulsion. In Sec. IV, we derive analytical expressions that approximate these energy changes and the intervals at which they occur. These expressions are the basis for a simplified simulation of ion cloud energy dynamics that avoids the computational overhead involved in tracking the motion of all ions in an rf field. We use the simplified simulation to investigate how various trap parameters affect rf heating. In Sec. V we experimentally validate our simulated results by a controlled melting of a two-ion crystal and estimate the ions’ energy change by monitoring changes in the cloud’s fluorescence.

II. HEATING IN TIME-DEPENDENT POTENTIALS: RF HEATING

In this section we give a general overview of the process of rf heating. We provide a qualitative description of the physical process involved in energy exchange between the rf field and an ion’s kinetic energy.

It is useful to describe the motion of trapped ions in two distinct timescales: rf motion (or *micromotion*), which describes the oscillation synchronous with the rf field, and *secular motion*, which describes the motion in a static harmonic potential, known as the *pseudopotential* [26]. The total energy of the ions can be separated into the energies corresponding to these two timescales:

$$E_{\text{tot}} = E_{\text{rf}} + E_{\text{sec}}. \quad (1)$$

The total system energy E_{tot} is the sum of contributions from the time-varying and static electric potential, the Coulomb interaction between ions, and the ions’ kinetic energy.

In the crystal phase, the secular and rf components of energy do not couple with each other. The secular energy E_{sec} is then conserved or well controlled, despite a time-dependent rf energy. In this regime, multiple co-trapped ions experience only small excursions from their respective trapping locations. Excursions are considered small if the ions’ deviations from their trapping locations are much smaller than the inter-ion separation in an ion crystal. The motion of the ions can then be expanded into normal modes of motion, with distinct frequencies and ideally negligible coupling. The secular modes of motion and micromotion have unique frequencies in separate timescales, and thus remain separated. In fact, when assessing the ions’ motion, micromotion is often neglected. In this secular approximation, the ions’ motion and energy are treated as if solely in an effective static harmonic potential, the pseudopotential.

In practice, undesired external influences can alter the ions’ secular energy. For example, particles from the residual background gas can collide with an ion. Such a collision can transfer enough energy to ions such that their range of motion exceeds the crystal’s inter-ion separation. Ions then undergo a transition to a melted state, an ion cloud. The motion of ions in a cloud is fundamentally different than in the crystal state. The average position of ions is fully governed by trap potentials, and not by Coulomb interaction. Furthermore, ions experience aperiodic motion due to irregular ion-ion Coulomb interactions. The frequency spectra corresponding to the secular motion and micromotion broaden and overlap due to this aperiodic motion. This allows energy from micromotion, E_{rf} , to be transferred to the secular motion E_{sec} . Therefore, unlike for an ion crystal, micromotion cannot be neglected when considering motion of ions in a cloud, and the pseudopotential approximation is no longer valid.

The energy transfer process from the rf-driven micromotion to the secular motion is known as rf heating, and is schematically outlined in one dimension in Fig. 2. In a static potential, two ions would approach each other, experiencing opposing Coulomb forces, and repel, as denoted by the dashed lines. In an oscillating potential, ions deviate approximately sinusoidally (solid lines) from this path. Since the strength of the rf field is dependent on the ions’ positions within the trap, the two ions experience different forces from the oscillating rf potential. In the example in Fig. 2, directly before the moment of closest proximity, the difference in relative velocity due to the rf force reduces the distance between the ions compared to the static potential. Ions therefore have more Coulomb energy at small distances than they would have in a static potential. As the ions begin to repel, the relative rf velocity has switched

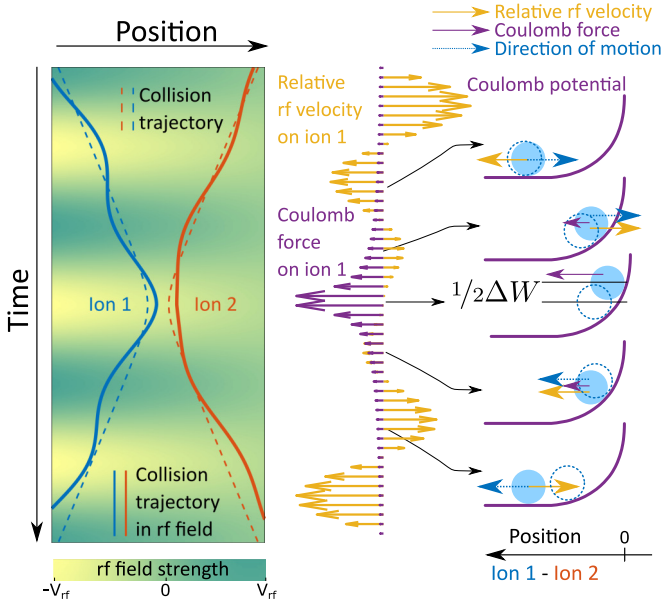


FIG. 2. Schematic of energy changes due to Coulomb interaction in an rf field. While following a trajectory governed by Coulomb repulsion, ions additionally experience an unequal force from the rf field, due to its position dependence. In this example, the rf phase is tuned such that, during the moments of increased Coulomb interaction, the relative rf velocity is aligned with the direction of motion, during both the approach and the withdrawal in the ions' motion. This leads to an increase of ΔW in motional energy after the collision. On the right, the solid circle represents the position of ion 1 as it increases and decreases in the Coulomb potential, whereas the dotted circle is the position if no rf is applied.

sign, and now the rf force aids in separating the ions. The extra relative secular velocity that the ions have gained by this time-varying force results in a gain in total energy in the ions' secular motion. The rf field has thus added energy (denoted as ΔW in Fig. 2) to E_{sec} . This process would remove energy from E_{sec} if the phase of the rf field had been shifted by π .

The schematic in Fig. 2 provides a qualitative description of the mechanism of energy transfer. In practice, such “head on” encounters do not occur in three dimensions, and the rf phase will generally not line up with the Coulomb force as schematically presented. In the following section, we simulate trapped-ion trajectories in a time-varying potential and assess rf heating in three dimensions.

III. FULL ION DYNAMICS SIMULATIONS

In this section, we investigate rf heating by analyzing simulations of particle dynamics of ion clouds. We numerically integrate the classical motion of charged particles by calculating forces given by a static (DC) field, a dynamic (rf) field, and Coulomb interactions. We refer to these simulations as “full” to contrast them with simplified simulations later in this work.

In our simulation, we track the dynamics of two trapped $^{40}\text{Ca}^+$ ions. We use trapping parameters that match typical experimental values [27], with motional frequencies of $\{\omega_x, \omega_y, \omega_z\} = 2\pi\{3.1, 3.4, 1.1\}$ MHz, where our coordinate system is chosen such that z corresponds to the direction with

no rf potential (axial) and x and y the two radial directions. The fields in the simulation are time-dependent quadrupole potentials. At the start of a simulation, ions are placed in their crystallized equilibrium positions. One ion is given an initial velocity in a random direction, mimicking a collision with a background gas particle. An initial kinetic energy of 1.4 meV is chosen, as it is marginally more than the required energy to melt the crystal [28]. This energy range corresponds to more than 10^5 motional quanta (≈ 16 K), so a classic evaluation of the equations of motion is justified. Laser cooling is not included in these simulations.

To investigate rf heating in these simulations, we determine the system's energy: In an ion cloud, each ion (with index i) has an energy given by the sum of its kinetic energy V_{kin} and its potential energy due to the trap's applied static and rf fields, V_{DC} and V_{rf} . Additionally, ions have energy due to the Coulomb interaction potential V_{Coul} between particles. The total energy E_{tot} in an ion trap system at any point in time t is thus given by

$$E_{\text{tot}} = \sum_i \left[V_{\text{DC}}(\vec{r}_i) + V_{\text{rf}}(\vec{r}_i, t) + V_{\text{kin}}(v_i) + \frac{1}{2} \sum_{j \neq i} V_{\text{Coul}}(\vec{r}_i, \vec{r}_j) \right] \quad (2)$$

for ions with positions \vec{r}_i and velocities v_i . The kinetic energy for an ion with mass m_i is given by $V_{\text{kin}} = (1/2)m_i v_i^2$. The Coulomb interaction energy V_{Coul} between particles i and j with charge q_i and q_j is given by

$$V_{\text{Coul}}(\vec{r}_i, \vec{r}_j) = \frac{1}{4\pi\epsilon_0} \frac{q_i q_j}{|\vec{r}_i - \vec{r}_j|}, \quad (3)$$

with the vacuum permittivity ϵ_0 .

We calculate the energy of the simulated system, E_{tot} , by inserting the numerically obtained ion positions and velocities into Eq. (2). However, the relevant quantity of energy is the secular component of E_{tot} in Eq. (1), as rf heating is defined by changes in this secular energy. To calculate the secular energy E_{sec} from the particles' simulated positions and velocities, Eq. (2) is adjusted in two ways:

(1) The rf potential $V_{\text{rf}}(\vec{r}_i, t)$ is replaced with the time-averaged field as experienced by the ions, the pseudopotential, which is an effective static potential $V_{i,\text{ps}}$ given by

$$V_{i,\text{ps}}(\vec{r}_i) = \frac{q^2}{4m_i\Omega_{\text{rf}}^2} |\nabla V_{\text{rf},0}(\vec{r}_i)|^2 \quad (4)$$

for an rf drive with position-dependent rf potential amplitude $V_{\text{rf},0}(\vec{r}_i)$ and frequency Ω_{rf} . For clarity, this potential is used as a means to extract the secular energy from simulation data, and is not used in the simulation itself.

(2) The positions and velocities of the ions, \vec{r}_i and \vec{v}_i , are replaced with their secular components, $\vec{r}_i^{(\text{sec})}$ and $\vec{v}_i^{(\text{sec})}$. These components are found by removing the rf component from the simulated positions $\vec{r}_i^{(0)}$, as follows: If the secular frequency $\omega_{\{x,y\}}$ is much lower than the rf drive frequency Ω_{rf} , the rf component of position, $\vec{r}_i^{(\text{rf})}$, can be described by

the equation of motion

$$\frac{d^2 \vec{r}_i^{(\text{rf})}}{dt^2} \approx -\frac{q \nabla V_{\text{rf},0}(\vec{r}_i^{(\text{sec})})}{m} \cos(\Omega_{\text{rf}} t). \quad (5)$$

This approximation is valid if the amplitude of $\vec{r}_i^{(\text{rf})}$ in one oscillation period is small enough such that $\nabla V_{\text{rf},0}(\vec{r}_i^{(\text{sec})})$ is approximately constant. Simulations do not directly provide $\vec{r}_i^{(\text{sec})}$, so we use an iterative approach and initially use the simulated positions $\vec{r}_i^{(0)}$ as an approximation for the secular motion: $\vec{r}_i^{(\text{sec})} \approx \vec{r}_i^{(0)}$. The rf component of the position is then

$$\vec{r}_i^{(\text{rf})} \approx -\frac{q \nabla V_{\text{rf},0}(\vec{r}_i^{(0)})}{m \Omega_{\text{rf}}^2} \cos(\Omega_{\text{rf}} t). \quad (6)$$

The secular motion is iteratively approximated by removing the rf component from the full simulated positions:

$$\begin{aligned} \vec{r}_i^{(1)} &= \vec{r}_i^{(0)} - \vec{r}_i^{(\text{rf})} \\ &= \vec{r}_i^{(0)} + \frac{q \nabla V_{\text{rf},0}(\vec{r}_i^{(0)})}{m \Omega_{\text{rf}}^2} \cos(\Omega_{\text{rf}} t). \end{aligned} \quad (7)$$

As $\vec{r}_i^{(1)}$ is a better approximation for secular motion than $\vec{r}_i^{(0)}$, we can improve our estimate for $\vec{r}_i^{(\text{rf})}$ in Eq. (6). Higher-order adjustments to the secular position can thus be found iteratively:

$$\vec{r}_i^{(n+1)} = \vec{r}_i^{(0)} + \frac{q \nabla V_{\text{rf},0}(\vec{r}_i^{(n)})}{m \Omega_{\text{rf}}^2} \cos(\Omega_{\text{rf}} t). \quad (8)$$

Note that Eq. (8) remains an approximation for the secular motion and is not an exact solution even as $n \rightarrow \infty$.

Figure 3(a) demonstrates how a simulated trajectory (projected in one dimension) is adjusted using Eq. (8) in several iterations to remove the rf component of its motion. The remaining motion is approximately secular. The trajectories $\vec{r}_i^{(2)}$ and $\vec{r}_i^{(3)}$ are visibly indistinguishable in Fig. 3(a). We find that \vec{r}_i^n changes negligibly for orders higher than $n = 3$.

Using $\vec{r}_i^{(n)} \approx \vec{r}_i^{(\text{sec})}$, the corresponding velocities $\vec{v}_i^{(n)}$, and the pseudopotential approximation $V_{i,\text{ps}}$, Eq. (2) can be adapted to calculate E_{sec} for each time step of the full simulation:

$$\begin{aligned} E_{\text{sec}} = \sum_i \left[V_{\text{DC}}(\vec{r}_i^{(n)}) + V_{i,\text{ps}}(\vec{r}_i^{(n)}) \right. \\ \left. + V_{\text{kin}}(v_i^{(n)}) + \frac{1}{2} \sum_{j \neq i} V_{\text{Coul}}(\vec{r}_i^{(n)}, \vec{r}_j^{(n)}) \right]. \end{aligned} \quad (9)$$

In this work, when describing the ion cloud's energy, we refer to the secular energy, E_{sec} , with $n = 3$.

Figure 3(b) shows traces of the energy E_{sec} over time, for several simulation runs. All simulations start with identical parameters, except for a randomly chosen rf phase, which reflects that a collision with a background particle can occur at any time during the rf drive cycle. In every trace, energy increases over time, but not necessarily continuously. Although the only difference between the individual simulations is the

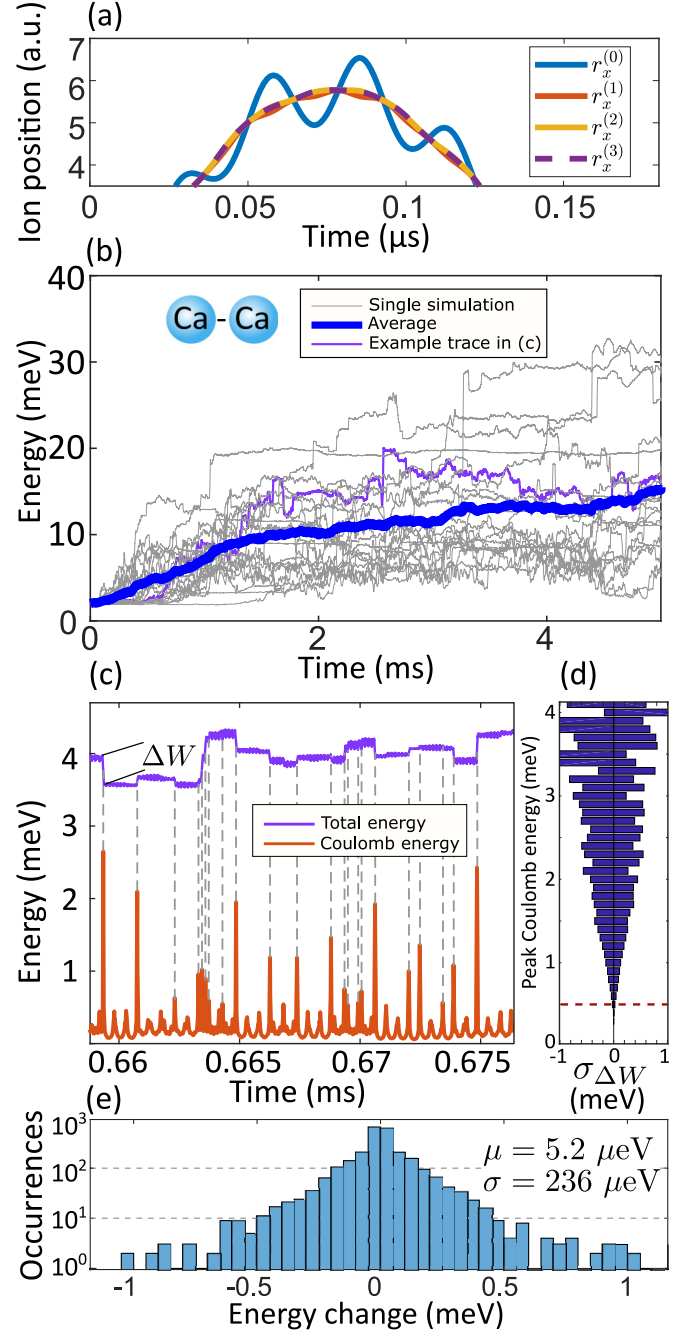


FIG. 3. Analysis of energy in Ca-Ca cloud dynamics simulations. (a) To extract the nondynamic component of energy, the rf component of the ions' motion is numerically removed. The rf-free motion is used to calculate the secular energy, E_{sec} . (b) The development of total energy is shown (thin lines) for several simulation runs, with identical starting energies. The thick blue line is an average of the individual runs. (c) Close-up of an energy trace for one simulation, marked in (b). The discrete changes in energy (ΔW) correspond to moments of high Coulomb interaction, i.e., collisions. (d) Standard deviation of energy changes $\sigma_{\Delta W}$ in bins of peak Coulomb energy, and (e) histogram of the magnitude of these energy changes, which have a mean of $\mu = 5.2 \mu\text{eV}$ and a standard deviation of $\sigma = 236 \mu\text{eV}$.

initial rf phase, there is a large variation in the development of energy over time, resulting in energies ranging from about 4 to 30 meV after 5 ms. This variation attests to the chaotic nature of melted ion dynamics.

The thick blue line is an average of the individual simulations, which increases approximately with the square root of time. To further examine the dynamics that lead to energy changes, we take a trace from Fig. 3(b) as an example and investigate it in Fig. 3(c).

Here, one can see that the secular energy does not change continuously, but at discrete points in time, corresponding to moments of increased Coulomb interaction. This behavior is ubiquitous over the full simulation duration of all traces, not just the example presented in Fig. 3(c). We refer to these moments of increased Coulomb interaction as *collisions*, since the interaction between the charged particles results in an exchange of momentum and energy. As described in Sec. II, this collision is inelastic, as secular energy is not conserved. We denote the individual changes in energy as a result of collisions by ΔW .

Figure 3(d) shows the standard deviation in ΔW , for various bins of peak Coulomb interaction energy. All traces in Fig. 3(b) are used for the statistics in Fig. 3(d). It is apparent that higher peak Coulomb interaction allows for a greater spread in resulting secular energy change. However, high Coulomb interaction does not always result in high changes in energy.

We observe that collisions with Coulomb interaction energies below 0.5 meV, indicated by the dotted line in Fig. 3(d), do not result in noticeable changes in the system's total energy. Thus, throughout this work, we will consider an ion-ion collision to be an event where the interaction energy exceeds this threshold.

Figure 3(e) shows the distribution of energy change which is qualitatively symmetric. However, the mean of the distribution $\mu = 5.2 \mu\text{eV}$ and average collision rate ($\bar{f}_{\text{coll}} = 528$ collisions per millisecond) lead to an overall increase of energy of approximately 14 meV after 5 ms of rf heating.

The simulations show that rf heating is not a continuous process, but occurs at discrete moments of high Coulomb interaction energies, which we refer to as ion-ion collisions. In the following section, we model the energy change due to such a collision event, and the rate at which such events occur, to build a simplified model of rf heating.

IV. COLLISION MODEL

In this section, we provide a generalized quantitative description of the parameters involved in energy dynamics in rf heating. We use this description as a basis for a model that predicts energy changes in ion-ion collisions, and the rate at which these collisions occur. This allows us to assess the contribution of various trapping parameters to rf heating rates. The model is used to create an ion cloud energy dynamics simulation that is computationally more efficient than the full simulation used in the previous section. We limit the following discussion to a single-species, two-ion cloud, but the method can easily be extended to clouds of multiple mixed-species ions.

A. Model parameters

Although melted ions experience an interaction energy that depends on their distance, we have determined in the previous section that below a certain threshold of Coulomb energy, changes in secular energy are negligible. We thus consider the discrete events where the Coulomb interaction surpasses the threshold that is found empirically from the full simulation. We refer to such an event as a collision. We model the energy dynamics in two steps: (1) estimate the change of energy due to a collision, and (2) estimate the collision rate.

1. Collision energy

We have established in Sec. II that when a collision occurs, the rf field induces a change in secular energy. We draw on results from the full ion dynamics simulation presented in Sec. III to derive and validate a model that describes this energy change.

The change in energy, ΔW , of any dynamic system of particles i can be expressed in terms of the forces \vec{F}_i acting on the particles with velocities \vec{v}_i as

$$\Delta W = \int \sum_i \vec{F}_i \cdot \vec{v}_i dt. \quad (10)$$

In a Paul trap, the total force on the ions is the sum of static and rf fields and the Coulomb force, $\vec{F}_i = \vec{F}_i^{(\text{DC})} + \vec{F}_i^{(\text{rf})} + \vec{F}_i^{(\text{Coul})}$. The velocity of the ions can be expanded into the contributions of secular and rf motion, $\vec{v}_i = \vec{v}_i^{(\text{sec})} + \vec{v}_i^{(\text{rf})}$. As described in Sec. II, the Coulomb force enables the transfer of energy between the secular and rf motion. In the product expansion of $\vec{F}_i \cdot \vec{v}_i$ in Eq. (10), this transfer is reflected by changes in the components $\int \vec{F}^{(\text{Coul})} \cdot \vec{v}^{(\text{rf})} dt$ and $\int \vec{F}^{(\text{Coul})} \cdot \vec{v}^{(\text{sec})} dt$. When evaluated over the duration of a collision, these integrals are equal and opposite in value. This value is the energy transferred due to a collision. Rf heating, which is the change in secular energy due to Coulomb interaction in an rf potential, can thus be expressed as

$$\Delta W_{\text{sec}} = - \int \sum_i \vec{F}_i^{(\text{Coul})} \cdot \vec{v}_i^{(\text{rf})} dt. \quad (11)$$

One could equally well describe the change in secular energy by the development of the integral containing $v^{(\text{sec})}$. However, since secular energy is temporarily stored in E_{Coul} during a collision, this integral contains sharp peaks at moments of high Coulomb interaction. Equation (11) is thus a smoother, and therefore more intuitive, representation of ΔW_{sec} .

Using $\vec{F}_1^{(\text{Coul})} = -\vec{F}_2^{(\text{Coul})}$ for a two-ion collision, the change in energy reduces to

$$\Delta W_{\text{sec}} = - \int \vec{F}_1^{(\text{Coul})} \cdot \Delta \vec{v}^{(\text{rf})} dt, \quad (12)$$

with the difference in rf velocity between the two ions $\Delta \vec{v}^{(\text{rf})} = \vec{v}_1^{(\text{rf})} - \vec{v}_2^{(\text{rf})}$.

We apply the integral of Eq. (12) to numerical data of one of the full ion dynamics simulations from Sec. III, which enables us to validate Eq. (12). Figure 4(a) shows the energy development as the accumulation of $\Delta W + E_{\text{init}}$ (medium red line), with $E_{\text{init}} = 2$ meV to reflect the initial energy of the system. For reference, the total energy E_{sec} [see Eq. (9)] of

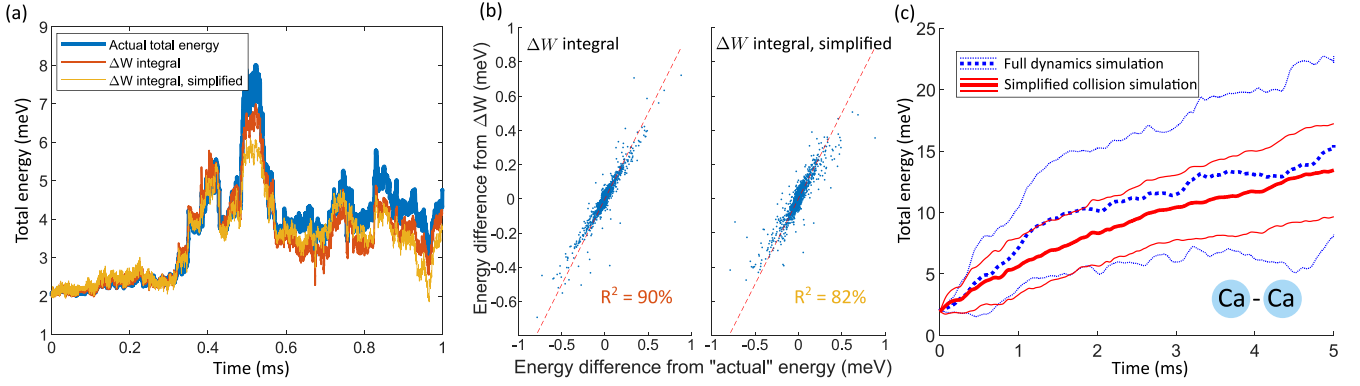


FIG. 4. Comparison of energy dynamics from the simplified model and full ion dynamics simulations. (a) The total energy of an ion dynamics simulation is shown in blue (thick line). The cumulative energy from Eq. (12) is shown in red (medium line). The thin yellow curve uses the approximated cumulative energy equation (19), with an rf-free trajectory. (b) Comparison of energy changes as determined from the calculated total energy with those from Eqs. (12) and (19). (c) The thick red line is the average of 20 simulation runs of the simplified energy gain model. The thin lines represent the standard deviation ($\pm\sigma$) of the individual runs. For comparison, the blue dashed curve shows the average energy from multiple full particle dynamics simulations.

the system is also plotted (thick blue line), showing close agreement. A comparison of the energy differences before and after collisions using the two energy metrics is shown in Fig. 4(b) (left). The calculated correlation between the two metrics (R-squared [29] of 90%) confirms that Eq. (12) can faithfully describe the change in secular energy.

Simplification of the energy transfer integral [Eq. (12)] can be achieved by approximating $\Delta\vec{v}^{(\text{rf})}$. The relative rf velocity $\Delta\vec{v}^{(\text{rf})}$ is estimated knowing the ions' positions relative to each other, and the phase of the rf field:

For a saddle-type rf potential

$$V_{\text{rf}}(\vec{r}_i, t) = \frac{1}{2}\psi_{\text{rf}}(r_{i,x}^2 - r_{i,y}^2) \cos(\Omega_{\text{rf}}t) \quad (13)$$

with potential curvature ψ_{rf} , the force on an ion i with charge q at position $\vec{r}_i = [r_{i,x}, r_{i,y}, r_{i,z}]$ is given by

$$\vec{F}_i^{(\text{rf})}(\vec{r}_i, t) = -q\nabla V_{\text{rf}} \quad (14)$$

$$= [-r_{i,x}, r_{i,y}, 0]q\psi_{\text{rf}} \cos(\Omega_{\text{rf}}t). \quad (15)$$

We have shown in Sec. III that we can approximate absolute changes in $r_{i,x}$ and $r_{i,y}$ to be constant during an oscillation cycle with frequency Ω_{rf} . Integrating $\int \vec{F}^{(\text{rf})} dt = m\vec{v}^{(\text{rf})}$ with mass m allows us to approximate the rf component of the velocity as

$$\vec{v}_i^{(\text{rf})} \approx [-r_{i,x}, r_{i,y}, 0] \frac{q\psi_{\text{rf}}}{m\Omega_{\text{rf}}} \sin(\Omega_{\text{rf}}t), \quad (16)$$

and the difference in rf velocity,

$$\Delta\vec{v}^{(\text{rf})} \approx [-\Delta r_x^{(\text{sec})}, \Delta r_y^{(\text{sec})}, 0] \frac{q\psi_{\text{rf}}}{m\Omega_{\text{rf}}} \sin(\Omega_{\text{rf}}t). \quad (17)$$

Here $\Delta r_x^{(\text{sec})}$ and $\Delta r_y^{(\text{sec})}$ are the ions' separation in their secular motion.

The Coulomb force is given by

$$F_1^{(\text{Coul})} = \frac{1}{4\pi\epsilon_0} \frac{q^2}{|\Delta\vec{r}|^3} \Delta\vec{r} \quad (18)$$

with $\Delta\vec{r} = \vec{r}_1 - \vec{r}_2$ the ions' separation, and ϵ_0 the vacuum permittivity. The Coulomb force $F_1^{(\text{Coul})}$ is dominated by the

secular motion of the ions, such that $\Delta\vec{r} \approx \Delta\vec{r}^{(\text{sec})}$. Equation (12) can thus be approximated as

$$\Delta W_{\text{sec}} \approx \frac{q^3\psi_{\text{rf}}}{4\pi\epsilon_0 m\Omega_{\text{rf}}} \int \frac{(\Delta r_x^{(\text{sec})})^2 - (\Delta r_y^{(\text{sec})})^2}{|\Delta\vec{r}^{(\text{sec})}|^3} \sin(\Omega_{\text{rf}}t) dt. \quad (19)$$

We numerically evaluate Eq. (19) using data from the full ion dynamics simulation. Results, shown in Fig. 4(a) (thin yellow line), are in agreement with the results generated with Eq. (12) (medium red line). The energy changes in these results are compared to energy changes derived from E_{sec} in Fig. 4(b) (right). From the correlation of the data shown in Fig. 4(b) (R squared of 82%), we conclude that Eq. (19) provides a good approximation of energy change in a collision. We thus have an expression that estimates secular energy changes due to collisions that relies on relatively little information about the trap and ions. Notably, to estimate the energy change, neither the ions' absolute position within the trap nor the rf components of their motion is required. The expression simply contains ions' relative position during a collision, and fixed trap parameters.

2. Collision rate

To predict the rate of energy change, we must determine the frequency at which collisions occur. The collision rate is estimated by calculating how often such events occur for particles with oscillatory motion in three dimensions (and no Coulomb interaction). Our method is outlined below.

We start by analyzing the one-dimensional case for two identical particles. The goal is to find the duration Δt_x that ions are within a chosen collision threshold r_c of each other within a secular oscillation cycle. We assume that the ions are moving sinusoidally at their secular frequencies. This is an approximation for ions that experience driven motion by the rf field. This additional driven motion is, however, not dominant: ion motion from simulations and analytic approximations in Sec. III show that for typical trapping parameters the amplitude of the rf-driven motion is less than 10% of the amplitude of the secular motion. Furthermore, the approximation is jus-

tified since the rf component of motion of the two ions is strongly correlated when they are within the collision range. Thus, the rf motion can be neglected when estimating the duration Δt_x . Additionally, collisions that lead to appreciable changes in energy occur near the center of the trap, where the amplitude of the rf-driven motion is minimal.

The positions of ions 1 and 2 are sinusoidal in time, with amplitudes $a_{1,x}$ and $a_{2,x}$, and a relative phase ϕ_x . The motion of the two ions is thus given by $r_{1,x} = a_{1,x} \sin(\omega_x t)$ and $r_{2,x} = a_{2,x} \sin(\omega_x t + \phi_x)$, with the oscillation frequency ω_x . The distance $d_x = a_{d,x} \sin(\omega_x t + \phi_{d,x})$ between the two ions is sinusoidal, with amplitude and phase

$$a_{d,x} = \sqrt{a_{1,x}^2 + a_{2,x}^2 - 2a_{1,x}a_{2,x} \cos(\phi_x)}, \quad (20)$$

$$\phi_{d,x} = \tan^{-1} \left(\frac{-a_{2,x} \sin(\phi_x)}{a_{1,x} - a_{2,x} \cos(\phi_x)} \right). \quad (21)$$

Using $t = 1/\omega_x (\sin^{-1}(d_x/a_{d,x}) - \phi_{d,x})$, the amount of time Δt_x that the two particles are within collision range r_c is

$$\Delta t_x = t(d_x = r_c) - t(d_x = -r_c) \quad (22)$$

$$= \frac{2}{\omega_x} \sin^{-1} \left(\frac{r_c}{a_{d,x}} \right). \quad (23)$$

In one dimension, noninteracting particles will be within collision range exactly twice per secular oscillation period (or be continuously within range). The collision criterion of $|d_x| < r_c$ can thus be represented by a pulse wave (a periodic rectangular function):

$$B_x(t) = \begin{cases} 1 & \text{if } (t \bmod T_x) < \Delta t_x \\ 0 & \text{otherwise,} \end{cases} \quad (24)$$

with period $T_x = \pi/\omega_x$. If $r_c > a_{d,x}$, Δt_x exceeds T_x , which is unphysical. Analytically, this results in B_x being continuously 1, which is physically accurate.

This model can be extended to three dimensions with three pulse waves $B_{\{x,y,z\}}(t)$, characterized by periods $T_{\{x,y,z\}}$ and pulse durations $\Delta t_{\{x,y,z\}}$. The collision rate is described by the average pulse rate of the product of the three pulse waves, $B_x B_y B_z$, and is given by

$$\bar{f}_{\text{coll}} = \frac{\Delta t_x \Delta t_y \Delta t_z}{T_x T_y T_z} \left(\frac{1}{\Delta t_x} + \frac{1}{\Delta t_y} + \frac{1}{\Delta t_z} \right) \quad (25)$$

and average time between collisions $\bar{t}_{\text{coll}} = 1/\bar{f}_{\text{coll}}$ (see Appendix A).

The condition that the three functions have an overlap ensures that the positions of the two ions are both within the bounds of a cube of side length r_c , but not necessarily that the two ions are within a distance r_c of each other. This is taken into account in our rf heating rate model, discussed in the following section.

B. Simplified rf heating model

In the previous section, we described the energy dynamics of melted ions by deriving models for ion-ion collision rates and associated energy changes. In this section, we use these models to construct a simplified rf heating simulation in which we repeatedly generate a time until a collision occurs, t_{coll} [Eq. (25)], followed by a change in energy due to that

collision, ΔW_{sec} [Eq. (19)]. The simplified simulation allows us to generalize our investigation of rf heating without the computational overhead inherent in the full ion dynamics simulation. The simplified simulation is outlined below.

As in the previous section, we describe the rf-free motion of the ions i as sinusoidal in three orthogonal directions (indexed k), with parameters $a_{1,k}$ and $a_{2,k}$ the amplitudes of ions 1 and 2, and relative phases ϕ_k . The energy of the system, conserved as long as a collision does not occur, is

$$E_{\text{sec}} \approx \sum_{i,k} \frac{1}{2} m \omega_k^2 a_{i,k}^2. \quad (26)$$

The approximation is based on the assumption that the Coulomb energy is negligible while ions are far outside of the collision threshold. The simulation is initialized with a chosen energy E_0 distributed randomly over the amplitudes $a_{i,k}$. The initial phases ϕ_k are chosen randomly and uniformly. The parameters $a_{i,k}$ and ϕ_k characterize the state of the ions between collision events.

Applying these parameters to Eqs. (23) and (25) yields a collision rate \bar{f}_{coll} . The collision threshold is chosen to be $r_c = 1.44 \mu\text{m}$, corresponding to a Coulomb energy of 0.5 meV, based on analysis of simulations described in Sec. III. There we argue that Coulomb energies less than 0.5 meV do not lead to appreciable rf heating.

The time between collisions is usually longer than a typical secular motion period and can thus be assumed to be uncorrelated due to the aperiodic nature of collisions (see Appendix A). Therefore, the probability distribution for collision times can be modeled as an exponential distribution, $P(t) = \bar{f}_{\text{coll}} \exp(-t \bar{f}_{\text{coll}})$. A random number from a known probability distribution function $P(t)$ can be generated by drawing a random value p , uniformly between zero and 1, and transforming it with the inverse cumulative distribution function (ICDF) [30] of $P(t)$. A random time t_{coll} is thus generated from the ICDF of the exponential distribution, given by $-\ln(1-p)/\bar{f}_{\text{coll}}$.

Since subsequent collisions require a pause time of at least half an oscillation period, we do not consider generated collision times lower than this period. Therefore, if the chosen t_{coll} is less than $\min_k T_k$, a new collision time is randomly generated. The ions' oscillation amplitudes $a_{i,k}$ and phases ϕ_k remain unchanged until time t_{coll} , at which a collision occurs and they need to be updated to reflect a change in energy.

We update $a_{i,k}$ and ϕ_k by running a Coulomb collision simulation which generates a randomized collision trajectory, based on values derived from $a_{i,k}$ and ϕ_k . The results of the simulation, along with a randomized rf phase, are applied to Eq. (19) to generate an energy change ΔW . Based on the simulated trajectories and ΔW , a new set of parameters $a_{i,k}$ and ϕ_k is obtained.

The Coulomb collision simulation acts as follows: For a given set $a_{i,k}$ and ϕ_k , we determine the approximate velocity of the ions at the moment of impact. The secular velocity $\bar{v}_i = [v_x, v_y, v_z]$ of ion i is given by $v_{i,k} \approx a_{i,k} \omega_k \cos \theta_{i,k}$, assuming that the rf contribution to the velocity is negligible for modeling a collision event. $\theta_{i,k}$ is given by $\omega_k t$ and $\omega_k t + \phi_k$ for the two ions. Referring to Eq. (21) in Sec. IV A, the separation between ions is given by $d_k = a_{d,k} \sin(\omega_k t + \phi_{d,k})$.

During a collision, the ion separation is much smaller than the oscillation amplitude, $d_k \ll a_d$. We thus have $\omega_k t \approx -\phi_{d,k}$ during a collision (other solutions, which include integer multiples of π , can be dropped without loss of generality). $\theta_{i,k}$ can then be written as

$$\theta_{1,k} = -\tan\left(\frac{-a_{2,k} \sin \phi_k}{a_{1,k} - a_{2,k} \cos \phi_k}\right), \quad (27)$$

$$\theta_{2,k} = \theta_{1,k} + \phi_k, \quad (28)$$

from which we calculate \vec{v}_i .

We use the ions' velocities \vec{v}_i as parameters for the collision simulation, a numerical integrator in which the only force is the Coulomb interaction. Two particles are placed at random points in a box with side lengths r_c , denoting their positions as $\vec{\chi}_i^{(0)}$. Particles are taken out of collision range by moving them to positions $\vec{\chi}_i^{(\text{start})} = \vec{\chi}_i^{(0)} - \vec{v}_i t_s$. The time t_s is chosen to be $t_s = 8r_c / \max_{i,k} |v_{i,k}|$, where the value 8 is chosen so that ions are placed far enough from each other such that the Coulomb energy is far below the collision threshold at start of the simulation. $\vec{\chi}_i^{(\text{start})}$ and \vec{v}_i are starting parameters for the simulation. The simulation is carried out for a time $2t_s$, which provides the time-dependent positions $\vec{\chi}_i(t)$ of the ions as they collide. A change in energy ΔW is then calculated using Eq. (19). Since the collision time is uncorrelated with the phase of the rf field, we add a random phase to the argument of the sine.

The calculated change in energy, ΔW , is used to update the parameters $a_{i,k}$ and ϕ_k : The final velocities from the Coulomb collision simulation $v_{i,k}^{\text{fin}}$ are adjusted according to Eq. (19), ΔW . Expanding Eq. (19) into its two sum components, the terms containing $\Delta r_x^{(\text{sec})}$ and $\Delta r_y^{(\text{sec})}$ are used to adjust the values of $v_{i,x}^{\text{fin}}$ and $v_{i,y}^{\text{fin}}$. These adjusted velocities, together with the positions of the collision, $\chi_{i,k}$, are used to calculate a new set of $a_{i,k}$ and ϕ_i . With this updated set of parameters, a new collision time t_{coll} is generated. This process is repeated until the sum of all collision times exceeds the desired simulation duration. E_{sec} is calculated with Eq. (26), using the parameters $a_{i,k}$ from every step of the simulation, giving a time-dependent energy. The simplified simulation reduces the computation duration by nearly three orders of magnitude, compared to the full ion dynamics simulation, reducing the time required to obtain traces such as those in Fig. 3(b) from tens of minutes to several seconds.

This method of estimating the ion cloud energy readily expands towards more than two ions by extending the parameter set $a_{i,k}$ and $\phi_{i,k}$. In this case, a collision time $t_{\text{coll}}^{(i,j)}$ is generated for all combinations of ion pairs $i \neq j$, and the ion pair with the shortest collision time is selected to undergo a simulated collision. The parameters $a_{i,k}$ of the chosen ion pair, with phase difference $\phi_{i,k} - \phi_{j,k}$, are updated to reflect a collision between those two ions, using the method described above. This method is applicable if one assumes that collisions are predominantly between no more than two ions. We have determined from ion trajectory simulations (using typical experimental parameters) that for clouds of three, four, and five ions, about 3%, 4%, and 7% of collisions involve three or more ions. While these percentages depend on trap parameters and ion energies, they serve as an indication of how often a more-than-two-body collision can be expected to occur.

We compare the performance of the full and simplified simulation, with identical trap parameters as used for Fig. 3(b). The results of the two types of simulation are displayed in Fig. 4(c). The thick lines are averages of individual simulation runs. The average energy is in good agreement for the two simulations, though the simplified model underestimates the standard deviation of all simulation runs, shown by the thin lines, denoting one standard deviation. We have made similar comparisons for varying parameters such as motional frequencies and particle masses (not shown), and conclude that the simplified energy simulations work reliably as an indicator for average change in energy.

We use the simplified simulation to investigate various trapping parameters, shown in Fig. 5. Each trace is an average of 20 individual simulation runs, each with randomly generated initial parameters $a_{i,k}$ and ϕ_k , constrained by a fixed initial energy (3 meV), given by Eq. (26). Unless otherwise noted, the simulations use two $^{40}\text{Ca}^+$ ions, with motional frequencies of $\omega_{\{x,y,z\}} = 2\pi\{3.4, 3.3, 1.1\}$ MHz and a 35 MHz trap drive frequency. Figure 5(a) shows traces of energy dynamics for various radial motional frequencies. Lower radial motional frequencies, and therefore a lower rf voltage, result in a lower gain in energy for a melted crystal. This behavior is observed by many ion-trapping experiments, where purposefully lowering the radial confinement assists the refreezing of a melted ion crystal [31]. As displayed in Fig. 5(b), a change in the axial confinement has a less significant influence on the rate of energy change, compared to the radial frequencies. Figure 5(c) shows energy dynamics for various ion species, where the motional frequencies have been kept constant by adjusting the rf and DC fields accordingly. Higher masses result in a higher rate of energy change. Figure 5(d) shows the energy change for various numbers of ions. Clouds with multiple ions exhibit a larger increase in energy, as collisions are more frequent. The slower initial onset of energy increase at higher ion number is because the initial energy of 3 meV is quickly distributed over all the ions, and thus individual ions have lower average initial energies, resulting in less energetic collisions.

We generalize the results displayed in Fig. 5 into a single model: We draw an analogy between melted ion energy transfer and random-walk processes, such as diffusion due to Brownian motion. In such processes, randomized changes in a variable result in an increasing statistical uncertainty in time, characterized by a diffusion constant. In our model, the energy E_{sec} over time t follows a trend of $E \sim \sqrt{Dt}$, where D is the diffusion constant [32,33]. To determine the parameters of the diffusive model, we perform least-squares regressions between the model $E_{\text{sec}} = E_0 + \sqrt{Dt}$ and our data, where E_0 is the initial energy (3 meV). By estimating the diffusion constant D for various trap parameters, we derive a generalized expression for D , in terms of ion mass m , axial frequency ω_z , radial frequency ω_r , trap drive frequency Ω_{rf} , and number of ions, n .

We use a polynomial model for D :

$$D = am^b \omega_r^c \omega_z^d \Omega_{\text{rf}}^e n^f \quad (29)$$

with estimated parameters a through f , displayed in Table I.

This simple model provides an effective method to quantify the energy dynamics resulting from rf heating. Notably, this

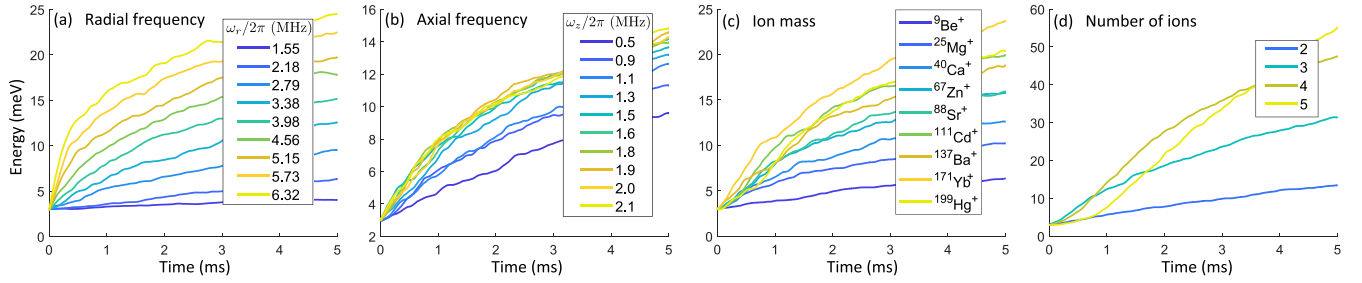


FIG. 5. Energy dynamics for a two-ion cloud for various trap parameters. Unless otherwise specified, plots use the following parameters: $m = 40$ amu, $\omega_z = 2\pi \times 1.1$ MHz, $\omega_r = 2\pi \times 3.3$ MHz, $\Omega_{\text{rf}} = 2\pi \times 35$ MHz. We vary (a) the radial motional frequencies, (b) the axial motional frequencies, (c) the ions' mass, and (d) the number of ions. In (c) the trapping fields are adjusted to ensure the same motional frequencies for all masses.

model is generally applicable to any linear Paul trap, and is easily applied by inserting known trapping parameters. Additionally, the model can be used to estimate an ion cloud heating rate with $E'(t) \approx D/(2E(t))$ (this is valid under the assumption that the initial energy E_0 is small compared to E , which is generally the case, as can be seen in Fig. 5). Several general conclusions can be drawn from the model:

For a fixed number of ions, the diffusion coefficient is most sensitive to changes in the radial motional frequency ω_{rf} , reinforcing the notion that reducing this parameter in an ion trap experiment (by reducing the rf voltage) is the most effective method of reducing the rf heating rate. The heating rate is to a lesser extent dependent on the axial motional frequency: this term only affects the collision rate [Eq. (25)], and does not influence the magnitude of energy change [Eq. (19)]. The heating rate is strongly dependent on the number of ions in the cloud, due to the increased collision rate. This conclusion emphasizes the necessity of efficient recooling when operating with increasing numbers of ions in, for example, registers of qubits for quantum computation. In the following section we investigate recooling of melted ions.

C. Cooling dynamics

Typical ion trap experiments use Doppler cooling to extract energy from the ions, enabling them to become and remain crystallized in the presence of heating processes caused by electric field noise [34]. It is, however, often the case that the Doppler cooling parameters that cool ions close to the Doppler limit [35] are not suitable to efficiently remove energy from an ion cloud. If the rf heating rate, described in the previous sections, is higher than the Doppler cooling rate, recrystalliza-

tion will not occur. In this section, we estimate the Doppler cooling parameters that enable efficient recrystallization by implementing a simple cooling model into our simulations.

Doppler cooling is a stochastic photon absorption and emission process, typically spanning a manifold of many electronic levels. For example, a $^{40}\text{Ca}^+$ ion is typically Doppler cooled in an eight-level manifold using 397-nm and 866-nm light. For ions with energies that are orders of magnitude higher than the Doppler cooling limit, the stochastic dynamics of this eight-level system can be approximated with a time-averaged force acting on an effective two-level system. In our experiment, we typically blue-detune the 866-nm repump beam and apply an abundance of beam power. This helps avoid dark resonances [36] and allows us to approximate the eight-level system as an effective two-level system. For a two-level system, the Doppler cooling force on an ion with velocity \vec{v} is given by [37]

$$\vec{F}^{(D)} = \frac{\Gamma}{2} \frac{\Omega^2/2}{\Omega^2/2 + \Gamma^2/4 + (\delta - \vec{k} \cdot \vec{v})^2} \hbar \vec{k}, \quad (30)$$

with Γ the spontaneous decay rate, Ω the on-resonance coupling strength, δ the detuning of the Doppler beam from resonance (in radians per second), \vec{k} the beam's wavevector, and \hbar the reduced Planck constant.

The cooling force [Eq. (30)] can be included as an additional force in the full ion dynamics simulation discussed in Sec. III. We have compared this time-averaged force to a simulation with identical trap parameters where Doppler cooling is modeled by discrete changes in momentum due to absorption and emission of photons in a two-level system. Upon comparing the two simulations, we find that Eq. (30) is a valid approximation of the stochastic cooling process in ion clouds. Using a time-averaged force, however, offers a lower computational cost.

Doppler cooling dynamics can also be included in the simplified rf heating simulations. This allows for analysis of Doppler cooling parameters necessary for refreezing a melted ion chain, without the computational cost associated with full particle dynamics. Incorporating Doppler cooling in our energy gain model is not as straightforward as its inclusion in the full ion dynamics simulations, since the simplified model does not continuously track time-dependent velocities, required for calculating $\vec{F}^{(D)}$. We implement Doppler cooling into the simplified model as follows.

TABLE I. Fit results for rf-induced energy diffusion model ($E \sim \sqrt{Dt}$, $D = am^b \omega_r^c \omega_z^d \Omega_{\text{rf}}^e n^f$) [D] = eV²/s.

Parameter	Fit value	Uncertainty
a	330	80
b	1.0	0.05
c	2.45	0.05
d	0.52	0.04
e	0.00	0.06
f	2.96	0.04

As described in Sec. IV B, we determine the time between Coulomb collisions, t_{coll} , and then make an update in particle parameters $a_{i,k}$ and ϕ_k , based on the change in energy caused by that collision. Additional to this change, we include the change in energy due to the time-averaged Doppler cooling force:

$$\Delta W_D = \int \sum_i \vec{F}_i^{(D)}(\vec{v}_i) \cdot \vec{v}_i dt. \quad (31)$$

Here, we require an analytic expression for the ions' velocities \vec{v}_i . The changes in particle parameters $a_{i,k}$ due to the Doppler force are usually small between collisions, and thus they can be approximated as constant for this duration. We use this approximation to derive an analytical expression for the motion, and thus the velocities, of the ions.

An ion's motion is separable in three dimensions. Along the axial (rf-free) dimension, the ion's motion is purely secular, $r_z = a_z \sin(\omega_z t)$, and the velocity is $v_z = \omega_z a_z \cos(\omega_z t)$. Along a radial direction, the motion is composed of a secular and an rf component, $r_x = r_{x,\text{sec}} + r_{x,\text{rf}}$, with $r_{x,\text{sec}} = a_x \sin(\omega_x t)$. We find $r_{x,\text{rf}}$ by reversing the approximation of Eq. (7) in Sec. III, which removes rf from the motion of a particle to obtain secular motion. Using $\nabla V_{\text{rf},0} = \psi_{\text{rf}}[r_x, -r_y, 0]$ [see Eq. (13)], $\vec{r}^{(0)} = \vec{r}$, and $\vec{r}^{(1)} = \vec{r}^{(\text{sec})}$, Eq. (7) is rewritten as

$$r_x \approx \frac{r_x^{(\text{sec})}}{1 + \frac{q\psi_{\text{rf}}}{m\Omega_{\text{rf}}^2} \cos(\Omega_{\text{rf}} t)}. \quad (32)$$

The velocity of ion i is then given by the time derivative of the position,

$$v_{i,k} = \frac{\omega_k a_{k,i} \cos(\omega_k t)}{1 + f_k \cos(\Omega_{\text{rf}} t)} + \frac{a_{k,i} f_k \Omega_{\text{rf}} \sin(\omega_k t) \sin(\Omega_{\text{rf}} t)}{(1 + f_k \cos(\Omega_{\text{rf}} t))^2}, \quad (33)$$

with $f_{\{x,y\}} = q\psi_{\text{rf}}/(m\Omega_{\text{rf}}^2)$ and $f_z = 0$. In practice, secular motional frequencies ω_i are easier to measure than the rf field curvature ψ_{rf} , so it is useful to rewrite f in terms of motional frequencies, as $f_{\{x,y\}} = \sqrt{\sum_k \omega_k^2}/\Omega_{\text{rf}}$.

The analytical expression for ion velocities is used in Eq. (31) to calculate the change in energy induced by the Doppler cooling beam. Values of $a_{i,k}$ are adjusted accordingly before each collision.

Results of our simulations of Doppler cooling an ion cloud, with Rabi frequencies (coupling strength) $\Omega/2\pi$, ranging from 0 to 80 MHz, are shown in Fig. 6(a), for a detuning of $\delta/2\pi = -40$ MHz. The wavevector is chosen to be $\vec{k} = (2\pi/\lambda)[0.07, 0.71, 0.71]$, with $\lambda = 397$ nm, which reflects the wavelength and angle of incidence in our experimental setup. We choose an initial energy of 15 meV, which is a typical ion cloud energy after 5 ms of rf heating. The thick lines in Fig. 6(a) are averages of 20 simulation runs, and the thin lines are the standard deviation of all runs. Results from the simplified simulation are compared to results from the full dynamics simulation with identical trapping and cooling parameters (dotted lines). As in the previous section, the average trends of the two simulations are in good agreement, although the simplified model underestimates the total spread of energy

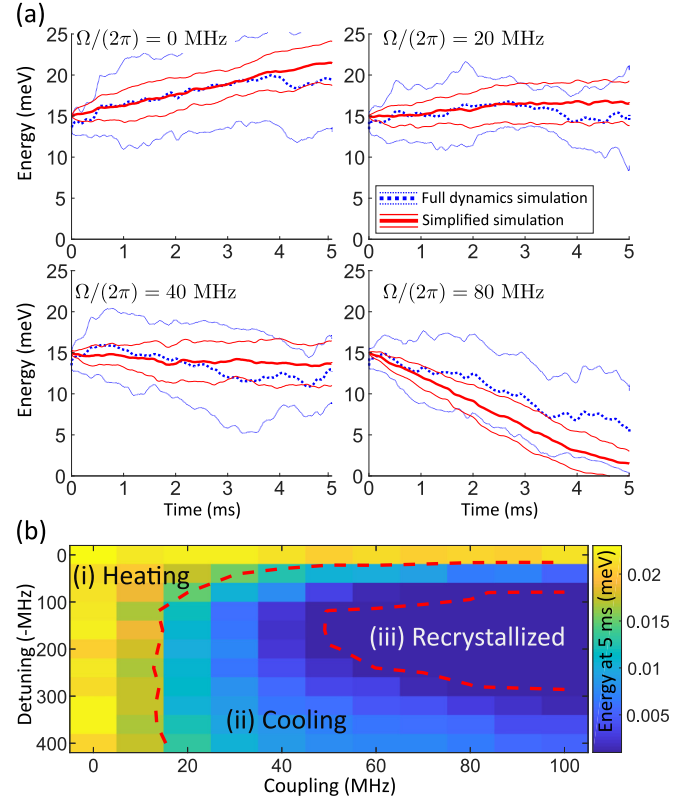


FIG. 6. Simulated energy dynamics with Doppler cooling. (a) Ca-Ca cloud energy as function of time, for various Doppler cooling coupling strengths, with detuning $\delta/2\pi = -40$ MHz. For comparison, results from both the full ion dynamics simulation and the simplified energy change simulation are displayed. The thick line is an average of multiple simulation runs, and the thin line represents the standard deviation of the individual runs. (b) Energy after 5 ms of Doppler cooling for varying cooling strengths and detunings. For Doppler cooling parameters corresponding to regime (i), the rf heating rate is higher than the Doppler cooling rate, and recrystallization will never occur. In both (ii) and (iii), the cloud's energy is decreased, but only in (iii) are the ions recrystallized after 5 ms.

in individual runs. The various plots show that with increasing coupling strength, the Doppler cooling rate overcomes the rf heating rate.

Figure 6(b) shows the simulated cloud (or crystal) energy after 5 ms of rf heating and simultaneous Doppler cooling, as a function of Doppler coupling strength Ω and detuning δ . The initial conditions for these simulations are the same as those in Fig. 6(a) (i.e., initial energy of 15 meV). The figure is subdivided into three regions: in region (i) the final energy is higher than initial energy, and in regions (ii) and (iii) the final energy is lower than the initial energy. In region (iii), the final energy is low enough for the ions to recrystallize.

Although the results in Fig. 6 are specific for the chosen trap parameters, they are indicative of the magnitudes of Doppler cooling parameters required for efficient recrystallization. For example, if ions are Doppler cooled continuously, recrystallization is achieved only if $\Omega \gtrsim \Gamma \approx 2\pi \times 20$ MHz and $\delta \gtrsim 2\pi \times 20$ MHz. In typical experimental sequences such as those used for ion-based quantum computation, ions are not Doppler cooled continuously, but are separated by

periods of noncooled computation steps. If Doppler cooling is not efficient enough to recrystallize an ion cloud before these steps, the cloud subsequently reheats in the duration that the cooling beam is off. In such a cycle, ions can indefinitely remain melted. Therefore, in such sequenced experiments, the range of Doppler cooling parameters that ensure recrystallization is more stringent, corresponding to region (iii) in Fig. 6(b).

V. EXPERIMENTAL VALIDATION

We validate the simulation methods with experimentally measured ion cloud energy dynamics due to rf heating and Doppler cooling. The goal is to demonstrate that low-energy clouds undergo significant changes at the millisecond timescale, and thereby reproduce the simulated results. In our experiments, we deterministically generate ion clouds and infer their energy dynamics by monitoring their fluorescence.

Our experiments are performed on two $^{40}\text{Ca}^+$ ions, in a surface Paul trap (see Fig. 1, lower panel). Fluorescence detection and Doppler recoiling is done by off-resonantly exciting the $4S_{1/2} \leftrightarrow 4P_{1/2}$ transition, at 397 nm. Undesired decay from $4P_{1/2} \rightarrow 3D_{3/2}$ is repumped with light at 866 nm. We model the cooling with an effective two-level coupling strength Ω and detuning δ , calibrated using Eq. (30) with measured fluorescence. This fluorescence is proportional to the magnitude of the Doppler cooling force of Eq. (30). The power and frequency of the 397-nm light are tunable parameters, whereas the 866-nm power and wavelength are kept constant. The effective spontaneous decay rate Γ is assumed to be dominated by the decay rate of the $4P_{1/2} \rightarrow 4S_{1/2}$ transition for $^{40}\text{Ca}^+$, and is thus $\Gamma = 2\pi \times 21.6$ MHz [38].

To deterministically generate a low-energy cloud, starting from a crystal, we exert a periodic force on the ions by applying an oscillating voltage on the trap electrodes, near resonance with the two radial motional frequencies, colloquially termed “tickling” [39]. We use a *two*-tone signal, since ions excited in the two radial dimensions require less total energy to undergo a phase transition into a cloud, compared to excitation in one dimension. The initial cloud energy is thus lower, allowing a more accurate analysis of the cloud’s energy gain. The rf tones are detuned from the motional mode frequencies by about -100 kHz. This helps to avoid recoiling the crystal before it melts: Motional frequencies in our anharmonic trapping potential decrease with increasing oscillation amplitude. The oscillation frequency of ions therefore approaches resonance with the excitation field as the ions’ motional energy increases.

In our experiment, we induce an oscillating electric field near the trapping region by superimposing the tickle pulse with the rf trap drive. The rf electrodes do not produce a field at the minimum of the pseudopotential, where ions are ideally located. We therefore apply a bias field of about $\nabla V_{\{x,y\}}^{(\text{bias})} = 100$ V/m in both radial directions, which displaces the ions from the trapping center, improving their coupling to the tickle field. This bias field displaces ions by $\Delta r_{\{x,y\}} = q\nabla V_{\{x,y\}}^{(\text{bias})} / (m\omega_x^2)$ from the trap center, which is less than a micrometer in our setup, and is negligible when considering melted ion dynamics.

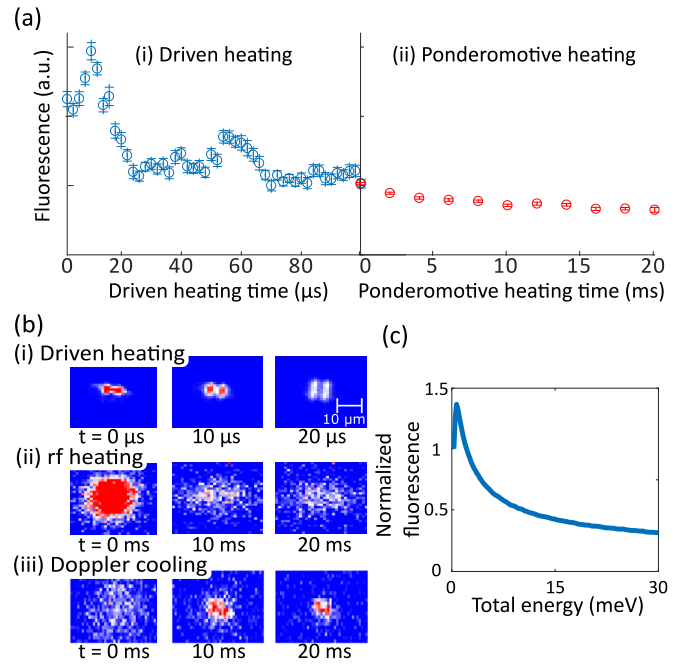


FIG. 7. The Ca-Ca ion cloud energy dynamics experiments, in which ion fluorescence is monitored using (a) a PMT and (b) a CCD camera. An experimental sequence is divided into three steps: (i) A tickle pulse excites the crystallized ions and induces enough energy to cause the crystal to melt. This is indicated by a drop in fluorescence. On the CCD camera, the two ions are no longer resolved. (ii) During an idle period, the rf field induces heating. This is detected as a drop of fluorescence and a dispersion of the cloud. (iii) Recooling the cloud with a Doppler beam reduces the cloud size and recrystallizes the ions. (c) The fluorescence rate is simulated as a function of ion energy, which allows us to interpret the measured fluorescence in terms of ion energy.

We determine from particle dynamics simulations that roughly 5–10 meV of energy is required to melt an ion crystal when exciting it in two dimensions. In our experiment, we observe the melting by a drop in fluorescence count rate of a detection pulse, measured with a photomultiplier tube (PMT). In addition to the PMT counts, we also monitor the fluorescence on a CCD camera, providing a spatial distribution of fluorescence. The detection time must be short enough to avoid a significant change in cloud energy during the detection period. Short detection times, however, result in a lower signal-to-noise ratio in the fluorescence count rate. We choose a detection time of $500 \mu\text{s}$ as a trade-off. As the fluorescence rate of an ion cloud in our experiment is on the order of 10^3 counts per second, we detect only a few counts per sequence cycle. We thus take an average count rate from >1000 repetitions of the sequence.

Figure 7(a), case (i), displays an example of detected fluorescence in terms of PMT counts, as a function of duration that the ion crystal is exposed to the tickle field. Figure 7(b), case (i), shows corresponding CCD images (averaged over multiple shots). In these images, the horizontal axis is the axial direction, and the vertical axis is a radial direction, parallel to the trap plane. After melting, the two ions are no longer individually resolved on the CCD image.

The total energy of the ion cloud directly after melting depends on the frequencies, amplitudes, and durations of both tickling pulses, and is difficult to predict exactly. Thus, in our results we do not control the initial energy of the ion cloud. However, stability in the rate of fluorescence in our measurements indicates that the average initial energy remains stable for the duration of the experiments with a fixed set of tickling signal settings.

After melting, we allow the cloud to evolve for a fixed duration, during which the ions undergo rf heating dynamics. After the evolution time, the fluorescence is probed with a PMT and camera. An example of such a measurement is shown in Fig. 7(a), case (ii), and Fig. 7(b), case (ii), where the fluorescence rate drops, and cloud size increases as a function of wait time, indicating an increase in cloud energy. We subsequently apply a 20-ms pulse of a high-power (>100 MHz), far-detuned (~ 120 MHz) Doppler cooling beam, which ensures that ions are recrystallized for following sequences.

The measured fluorescence count rates are to be mapped into estimated cloud energy. We find this relation through an independent simulation: A random set of oscillation amplitude parameters $a_{i,k}$ (see Sec. IV B) is generated for a given ion cloud energy E_{sec} . These amplitude parameters are used to calculate ion velocities $\bar{v}_{i,k}$ with Eq. (33) for times $t \in [0, t_{\text{max}}]$ with $t_{\text{max}} \gg 2\pi/(\min_k \omega_k)$. Inserting these velocities into Eq. (30) gives a time-dependent laser cooling force. The average force in the duration t_{max} is proportional to the fluorescence rate. Fluorescence rates are normalized to measured rates at zero energy. In the experiment, this corresponds to the rate of fluorescence detected from an unperturbed ion crystal (i.e., neither displaced by a radial offset field, nor excited by means of oscillating tickle field). The procedure of simulating the fluorescence rate is repeated 20 times with random sets of $a_{i,k}$, from which we take an average.

Normalized fluorescence rates are shown in Fig. 7(c) as a function of ion cloud energy. With this curve, a measured value of fluorescence can be used to extract the cloud energy. The mapping of fluorescence to ion energy is, however, not unique for the full domain. The measured energies, $E_{\text{sec}} > 5$ meV, are outside of this range of ambiguity for our parameters, $\Omega/2\pi = 64$ MHz and $\delta/2\pi = -40$ MHz. A decrease in fluorescence rate is thus correlated with an increase in energy.

Figure 8(a) shows the ion cloud energy, inferred from measurements, as a function of wait time, for various radial motional frequencies. These frequencies are adjusted by changing the power of the rf drive. The plotted points are the mean values of calculated energy, inferred from the >1000 repetitions of the sequence. The error bars represent the statistical uncertainty of the mean, but do not take possible systematic errors in converting fluorescence into energy into account. The dashed lines represent the lower and upper boundaries of the standard deviation of multiple simulation runs, using the simplified rf heating model presented in Sec. IV B. Measured and simulated data are in agreement for both the time evolution of energy and the motional frequency dependence.

We apply a Doppler cooling beam after allowing the crystal to gain energy, to investigate the recooling efficiency. Variable parameters are the beam's coupling strength Ω (varied by adjusting the beam power), the beam's detuning from reso-

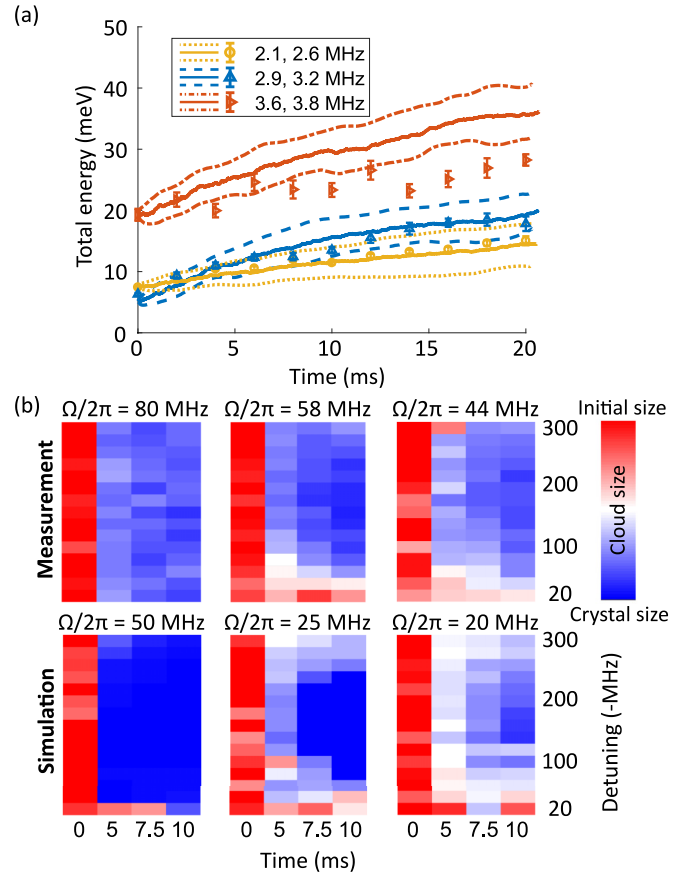


FIG. 8. Ca-Ca ion cloud energy dynamics experimental results. (a) Energy dynamics have been measured for three sets of radial motional frequencies. Error bars represent the statistical uncertainty in the acquired mean energy, but do not take into account systematic errors in converting fluorescence into energy. The thick lines are an average of simulated energies, and the thin lines are the standard deviation ($\pm\sigma$). (b) We measure the cloud size after Doppler cooling, using CCD imaged fluorescence. We scan the Doppler beam's detuning from resonance, effective coupling strength, and Doppler cooling time. The reduction in cloud size indicates a loss of cloud energy. The colors in the figure are scaled with the mean cloud size at 0 ms and crystal size as high and low references. Simulated cloud sizes are displayed below for comparison, shown at coupling strengths at which the residual differences between measurement and simulation are minimized.

nance, δ , and the cooling duration. As before, the energy of the cloud (or potentially crystal, after sufficient cooling) is probed with a short detection pulse. In our experiment, the detection pulse has the same coupling strength Ω and detuning δ as the cooling pulse, which means that we cannot measure the fluorescence rate independently of cooling parameters. We thus take CCD image data, and use the cloud size [using a two-dimensional (2D) Gaussian fit] as an indicator of cloud energy. Figure 7(b), case (iii), shows example images of an ion cloud decreasing in size with increasing recooling duration.

Figure 8(b) displays the measured time evolution of ion cloud size when Doppler cooling is applied. We investigate various coupling strengths $\Omega/(2\pi) = \{44, 58, 80\}$ MHz, at detunings ranging from $\delta/(2\pi) = -20$ to -300 MHz. Plotted

alongside are cloud sizes as determined from the simplified energy simulations (Sec. IV B), including Doppler cooling. In these simulations, we reconstruct the cloud size by calculating and correlating the ions' positions and fluorescence rates using the ion motion parameters $a_{i,k}$ within the respective detection window. Cloud images are simulated at the same detunings and times as used for the experimental results shown in Fig. 8(b). The simulations are run for various coupling strength parameters, ranging from 10 to 120 MHz. From this set, we extrapolate which value of simulation coupling strength has the best agreement with the displayed experimental data, in terms of least-squares difference. The simulation results with the best agreements are displayed alongside the respective experimental results in Fig. 8(b). The color scaling is chosen such that the two color extremes represent the average size of the initial cloud and of the crystallized ions, as detected by the CCD. We do not attribute an absolute pixel value to this scale, as the detected cloud size is dependent on cooling parameters. The perceived initial cloud size is therefore not identical for the various plots.

The simulated coupling strength values differ from the experimental values by about a factor of 2. We attribute this discrepancy to two causes:

(1) In our simulations, we do not correct for the spatial dependency of the power of the cooling beam, which is assumed to be uniform over the entire ion cloud. In the experiment, the beam diameter is estimated to be about 30 μm . At a total energy of 0.02 eV and 1 MHz axial frequency, ions typically undergo excursions of about $\pm 18 \mu\text{m}$ from the trap center. The spatial distribution of the Doppler beam is thus not negligible.

(2) The force from the Doppler cooling beam is approximated by a continuous force acting on a two-level system. In reality, this does not cover the full complexity of the stochastic forces that are described by the eight-level system. For example, in calibrating the coupling strengths Ω , we fit experimental data to a model that assumes a spontaneous decay rate of $\Gamma/2\pi = 21.6$ MHz, which neglects possible decay to the $3D_{3/2}$ electronic level. The modeled value of spontaneous decay Γ is thus an upper bound for the effective two-level spontaneous decay.

Barring the discrepancy caused by the approximations used in the simulations, from both the experimental and simulated data in Fig. 8(b) the conclusion can be drawn that efficient recrystallization of a Ca-Ca cloud is achieved in about 5 ms, using Doppler cooling with $\Omega/(2\pi) > 80$ MHz and $\delta/(2\pi) \approx 150$ MHz. Recrystallization is delayed or unattainable with a lower beam power and/or incorrect detuning.

VI. CONCLUSIONS

In this work we have considered the properties of rf heating in ion clouds in Paul traps. Using a simplified simulation, we have attained a generalized model to describe the rate of energy gain after ions have melted. This simple analytic equation estimates rf heating rates for low-ion-number clouds in linear Paul traps, for known trapping parameters. Experimental trials have confirmed the energy growth trends for a two-ion cloud, and have demonstrated requirements for cooling parameters for recrystallizing the ions.

The results convey the necessity of having a recrystallization setting in experimental hardware in addition to the typical trapping and Doppler cooling settings. A detuning of half the spontaneous decay rate of the cooled ion, $\delta = \Gamma/2$ is a commonly used value for Doppler cooling in ion trap experiments, since for low coupling, $\Omega \ll \Gamma$, this detuning yields the lowest energy [35]. Figure 7(c) shows that this detuning is not suitable for recrystallizing an ion cloud, as the rate of rf heating exceeds the rate of Doppler cooling. It is therefore common for experiments with crystals consisting of multiple ions to have a so-called refreeze beam—a high-power, far-detuned, Doppler cooling beam. While settings for such a beam are conceptually familiar, this work provides a quantitative description of the heating and cooling processes involved.

Efficiently overcoming rf heating is imperative in ion trap systems with low ion escape barriers, such as surface traps. Ion-trap-based quantum computers envision migrating towards segmented surface trapping architectures to realize scalability [40]. With increasing numbers of ions, collisions with background particles become more frequent, and therefore also the number of melting events. Even if the energy transferred in such collisions is lower than the trap depth of surface traps (typically tens or hundreds of meV), energy gain from rf heating can lead to loss of ions from the trap, possibly in tens of milliseconds. Therefore, to avoid persistently reloading ions, experimental sequences should include a refreeze phase in every cycle. Our results suggest that for recrystallization of a two-ion cloud, the Doppler cooling beam should have a detuning of roughly $\delta \approx -6\Gamma$ and should be applied for more than 5 ms, with at least $\Omega > 3\Gamma$ coupling strength. However, the simulations indicate that the conditions for recooling are more demanding with an increasing ion number. Lowering the power of the rf drive field during this refreeze phase will aid recrystallization by decreasing rf heating. Our results show that at a lower rf power, the benefit of a lower heating rate outweighs the disadvantage of the resulting lower trap depth.

The considerations of trap and cooling parameters become more stringent when considering mixed-species operation [41] in surface traps, whose use is also envisioned in ion-based quantum computers [42]. For single-species clouds in fixed trapping fields, rf heating rates decrease as the ions' mass increases. This can be seen in Table I, noting that for fixed trap parameters, $m \propto \omega_r^{-1}$. On the other hand, the trap depth, usually lowest in the radial direction perpendicular to the trap surface, is approximately proportionally lower for higher masses. Simulations show that mixed-species crystals suffer from a worst-of-both-worlds situation: rf heating rates are dominated by the lower mass ion in the cloud, while the trap depth remains low for the higher mass ion. This also limits the extent to which the rf drive power can be reduced without risking ion loss. It is therefore beneficial to operate ion traps with species of similar mass. However, regardless of the mixed-species mass ratio, efficient recrystallization is imperative.

In this work, we have analyzed a dynamic chaotic system and developed a simplified model to characterize it. The rf heating model can be further extended to include effects of multispecies operation, larger numbers of ions,

excess micromotion, and anharmonicities in trapping potentials. Furthermore, recrystallization with Doppler cooling can be further investigated, accounting for the effective dynamics of the eight-level cooling scheme. A Doppler beam with chirped detuning [43] can, for example, be an effective method to ensure recrystallization.

The data in this work are openly available at [44]. The full ion dynamics data in Figs. 3(b) and 4(a) are available upon reasonable request. The ion trajectory simulation code is available at [45].

ACKNOWLEDGMENTS

This research was funded by the Office of the Director of National Intelligence (ODNI), Intelligence Advanced Research Projects Activity (IARPA), through the Army Research Office Grant No. W911NF-16-1-0070. All statements of fact, opinions or conclusions contained herein are those of the authors and should not be construed as representing the official views or policies of IARPA, the ODNI, or the U.S. Government. We gratefully acknowledge support by the Austrian Science Fund (FWF), through the SFB BeyondC (FWF Project No. F7109-N38). We acknowledge support from the IQI GmbH.

APPENDIX A: DERIVATION OF 3D COLLISION RATE

In Sec. IV A, the motion of two ions is described as sinusoidal, with different amplitudes $\{a_i\}$ and frequencies $\{\omega_i\}$ in all three dimensions. In each dimension separately, ions are within collision range (such that the distance between ions, d_i , is below a given range r) twice per oscillation period, $2\pi/\omega_i$. This collision condition in one dimension is thus represented by a pulse wave $B_i(t)$, with period $T_i = \pi/\omega$ and pulse duration Δt_i , as in Eq. (24). We define a two-ion collision as an event where the collision condition is satisfied in all three dimensions simultaneously, given by the pulse wave $B_{3D}(t) = B_x B_y B_z$. As this three-dimensional pulse wave is aperiodic (the periods T_i are not rationally related), $B_{3D}(t)$ does not have a fixed pulse period. However, an *average* pulse period can still be defined, given by the average time between pulses. The collision rate \bar{f}_{coll} is then the average number of pulses in B_{3D} per time. In this section, we derive the average collision rate in B_{3D} as a function of pulse parameters T_i and Δt_i .

The probability that the 3D collision condition, $B_{3D}(t) = 1$, is met at any moment in time t is given by the product of the probabilities that $B_i = 1$ for $i = x, y, z$, $P_{3D} = \prod_i P_i$, with the one-dimensional (1D) probabilities $P_i = \Delta t_i/T_i$. Intuitively, the collision rate is given by the product of the momentary collision probability P_{3D} , and the effective rate at which P_{3D} is resampled.

We derive \bar{f}_{coll} with a geometric argument, depicted in Fig. 9 (shown in two dimensions, for clarity). The pulse wave $B_{2D}(t) = B_x(t)B_y(t)$ in Fig. 9(a) is a function of time t . The individual pulse waves B_x and B_y can, however, graphically be separated into two time dimensions, t_x and t_y , depicted in Fig. 9(b) as two time axes. The vertical and horizontal shaded regions correspond to regions where $B_x = 1$ and $B_y = 1$, respectively. The locations where the vertical and horizontal bars meet are places that satisfy the collision condition, $B_{2D} =$

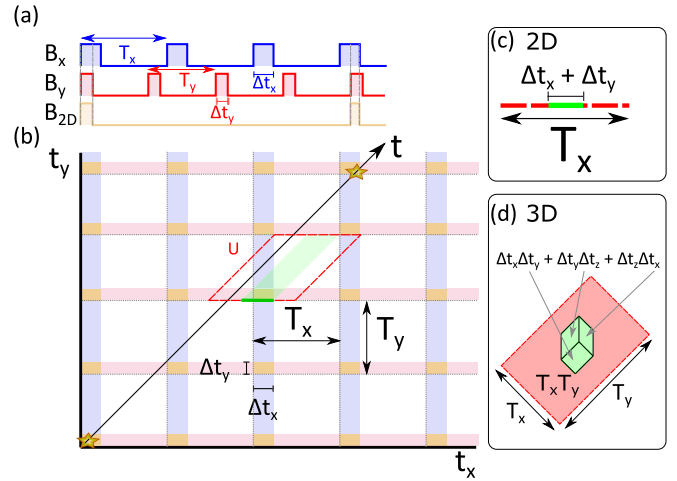


FIG. 9. Graphical representation of collision condition, for deriving the 3D collision frequency. (a) In dimensions x and y , the collision conditions are represented by pulse waves B_x and B_y . In two dimensions, a collision is represented by the nonperiodic pulse wave $B_{2D} = B_x B_y$. (b) $B_x(t)$ and $B_y(t)$ are displayed as two orthogonal temporal dimensions, such that their respective collision conditions are vertical and horizontal bars. “Real” time is the diagonal line $t_x = t_y$. Collisions occur where real time crosses vertical and horizontal bars simultaneously, denoted by the yellow boxes. This is equivalent to the real-time line crossing the green shaded area, the 45° projection of collision boxes in unit cells U . Therefore, in the example unit cell in (b), no collision occurs. The probability of a collision occurring in a unit cell is thus given by the ratio of the projection of the green region onto the base of the unit cell, and the base of the unit cell itself. This probability, schematically shown in (c) two dimensions and (d) three dimensions, is multiplied by the frequency that the time line enters new unit cells to give the collision frequency.

1. These are graphically represented by the yellow boxes, with side lengths Δt_x and Δt_y . “Real” time t parametrically follows the diagonal line, $t_x = t_y$. Whenever the real-time line crosses a yellow box, a collision occurs (starred regions).

We consider the parallelogram unit cell U (red dashed line), whose height is given by the lowest value of $\{T_i\}$ (in this example, the lowest value is T_y ; we see later that this choice is made without loss of generality), and a base width given by the remaining value (T_x). The parallelogram angle follows the real-time line t , at 45° . Each unit cell contains exactly one collision box. The collision box is projected at 45° through the unit cell, denoted by the green shaded area. Graphically, a collision occurs if the time line passes through this area, as the real-time line then has overlap with the collision box. In the example unit cell of Fig. 9(b), no collision occurs. Since T_x and T_y can be assumed to be irrationally related, the location where the time line enters a unit cell is uniformly distributed. Therefore, the probability of a collision occurring in a unit cell is given by the ratio of the green shaded area to the area of the unit cell. This is identical to the ratio of the lengths of the base of the green area to the base of the unit cell. The base of the green area is the projection of the collision condition box along the axis of the time line onto the base of the unit cell box (indicated by the thick green line). Since the projection is along a 45° angle onto the x axis, the length

of the projection is given by $\Delta t_x + \tan(45^\circ)\Delta t_y = \Delta t_x + \Delta t_y$. The probability that a collision occurs within a unit cell is therefore $P_{U,2D} = (\Delta t_x + \Delta t_y)/T_x$ [see Fig. 9(c)].

Extending this concept into three dimensions [see Fig. 9(d)], the base of the unit cell is now two dimensional, with an area of $A_U = T_x T_y$, assuming the shortest time in $\{T_i\}$ is T_z . The area of the projection of the collision box is given by $A_{\text{coll}} = \sum_i \sum_{j>i} \Delta t_i \Delta t_j$. The probability of a collision occurring within a unit cell is $P_U = A_{\text{coll}}/A_U$. Note that with this geometric argument P_U can exceed 1, and should be numerically capped off at this value. For typical experimental values of Δt_i and T_i it is generally the case that $P_U \ll 1$.

After passing through N unit cells, on average $n_{\text{coll}} = P_U N$ collisions have occurred. The time line enters a new unit cell at intervals T_z , so $N = t/T_z$. The collision rate is thus $\bar{f}_{\text{coll}} = n_{\text{coll}}/t = P_U/T_z$. Rewriting gives

$$\bar{f}_{\text{coll}} = \prod_i \left(\frac{\Delta t_i}{T_i} \right) \sum_i \frac{1}{\Delta t_i}, \quad (\text{A1})$$

which conforms with the intuition that the collision rate is given by the product of P_{3D} and an effective resample rate.

APPENDIX B: NUMERICAL ANALYSIS OF COLLISION TIME MODEL

In the simplified rf heating model presented in Sec. IV B, we update the ions' secular energy at intervals given by an estimated time t_{coll} between ion-ion collisions. To generate this time for a given set of ion and trap parameters, we first find an *average* collision time \bar{t}_{coll} , as given by Eq. (25). We then randomly sample from a truncated exponential distribution characterized by this average rate. In this Appendix, we analyze these methods through comparison with numerical simulations.

The average collision time \bar{t}_{coll} is a function of the ions' secular motion amplitudes $a_{i,k}$ (for ion i in direction k), and their relative motional phase ϕ_k . We generate a random set of these parameters [$a_{i,k} \in (0, 10^{-4})$ m, $\phi_k \in (0, \pi)$] and simulate the ions' time-dependent positions under the influence of the rf potential, though neglecting Coulomb interaction to ensure that the parameter set $a_{i,k}$ and ϕ_k remains unaltered for the duration of the simulation. We then query how often the collision condition is met, i.e., $|r_{1,k} - r_{2,k}| < r_c$, simultaneously for all $k = \{x, y, z\}$. The number of collisions occurring in the duration of the simulation gives us the simulated collision rate. We compare this collision rate with the analytically obtained collision rate given by Eq. (25). We repeat this method 20 times with randomly generated parameters, and plot the results in Fig. 10, which compares the simulated and analytically obtained average collision rate (triangles). We additionally repeat this process another 500 times, though we replace the ion dynamics simulation with an analytic expression for ion position, as given by Eq. (32), which greatly reduces the computation time per repetition (circles). Results in Fig. 10 show good agreement between simulations and the analytic model. The larger deviation at large collision times is attributed to larger statistical errors, as only a few collisions occur during the millisecond simulation time.

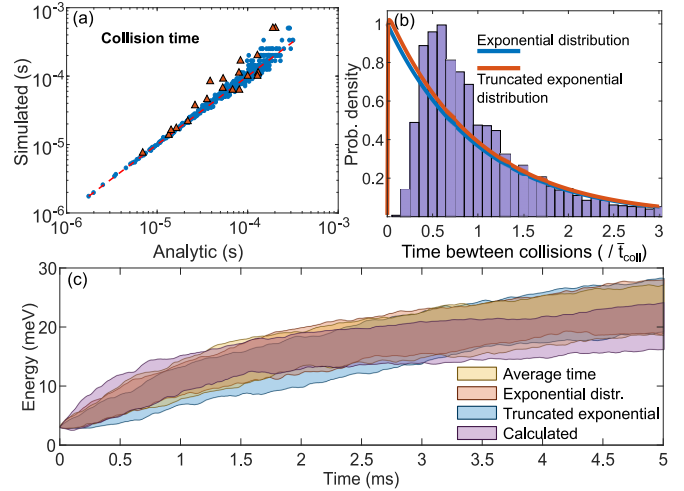


FIG. 10. Numerical analysis of collision time model. (a) Correlation plot of analytically and simulated obtained average collision times \bar{t}_{coll} for a randomized set of ion motion parameters $a_{i,k}$ and ϕ_k . The simulated data are derived from numerical ion dynamics simulations (triangles) and analytically approximated ion positions (circles). (b) Distribution of collision times, normalized to the average collision rate. For comparison, an (truncated) exponential distribution function is shown in blue (red). Various collision time strategies are used in the simplified rf heating simulation, of which the results are compared in (c).

After each collision event, a new collision time is to be determined. For this, one could simply use the average time \bar{t}_{coll} , since this suitably approximates the time over which rf heating occurs after thousands of collisions. However, we attempt to design our time selection procedure to be more physically accurate, without compromising the computation time of the simplified rf heating simulation. We do this by drawing a new time randomly from a distribution function, which is parametrized by the analytically obtained average collision time.

Designing a physically accurate description of the distribution function is mathematically cumbersome, given the aperiodic nature of the 3D collision criterion (see Appendix A). We thus aim to find a simplified approximation of the distribution function. In our work, we have chosen an exponential distribution based on the notion that the aperiodic collision conditions are uncorrelated events. This is a simplification, since after a collision occurs, a subsequent collision is more likely to occur close to a multiple of the three motional periods. Using the same randomized parameters as the results presented in Fig. 10(a), we obtain histogram bin counts of times between collisions, which are normalized to the numerically obtained *average* collision time. The resulting data are shown in Fig. 10(b). For comparison, an exponential distribution function is plotted. There is a good agreement at longer ($> \bar{t}_{\text{coll}}$) collision times, but qualitatively less overlap at lower times. Regardless, this method represents a computationally inexpensive improvement over simply selecting the average time \bar{t}_{coll} as a new collision time. A further improvement is made by assuming that the minimum time between collisions is required to be at least one-half oscillation period (T_k in the main text). This restriction is imposed by rejecting

and resampling the randomly generated collision times, effectively truncating the exponential distribution function. This truncated distribution is also shown in Fig. 10(b).

Ultimately, the main performance check is comparing the simplified simulation to the full ion dynamics simulation, as in Fig. 4(c). We can also compare the performance of the simplified simulation using various strategies for generating new collision times, using (1) the analytically obtained average time directly without sampling from a distribution, (2) sampling from an exponential distribution characterized by the average time, (3) sampling from a truncated exponential distribution, and (4) simulating ion positions after a collision

to determine the time of the next collision. The energy dynamics of the simplified simulation with these strategies are shown in Fig. 10(c), where each shaded region represents the standard deviation around the mean ($\mu \pm \sigma$) of 50 simulation runs for each strategy. The change in energy is similar for all methods. However, the simulated ion position approach has significantly more computational overhead. In our work we elect to use the truncated exponential distribution function. While sampling from this distribution does not lead to a notable improvement of the simulation results compared to using the average time, it depicts a more accurate physical representation, at nearly no extra computational cost.

-
- [1] D. Leibfried, R. Blatt, C. Monroe, and D. Wineland, Quantum dynamics of single trapped ions, *Rev. Mod. Phys.* **75**, 281 (2003).
- [2] G. Araneda, D. B. Higginbottom, L. Slodička, Y. Colombe, and R. Blatt, Interference of Single Photons Emitted by Entangled Atoms in Free Space, *Phys. Rev. Lett.* **120**, 193603 (2018).
- [3] C. Monroe, D. M. Meekhof, B. E. King, and D. J. Wineland, A “Schrodinger cat” superposition state of an atom, *Science* **272**, 1131 (1996).
- [4] N. Poli, C. W. Oates, P. Gill, and G. M. Tino, Optical atomic clocks, *Riv. Nuovo Cimento* **36**, 555 (2013).
- [5] D. J. Douglas, A. J. Frank, and D. Mao, Linear ion traps in mass spectrometry, *Mass Spectrom. Rev.* **24**, 1 (2005).
- [6] C. D. Bruzewicz, J. Chiaverini, R. McConnell, and J. M. Sage, Trapped-ion quantum computing: Progress and challenges, *Appl. Phys. Rev.* **6**, 021314 (2019).
- [7] S. Debnath, N. M. Linke, C. Figgatt, K. A. Landsman, K. Wright, and C. Monroe, Demonstration of a small programmable quantum computer with atomic qubits, *Nature (London)* **536**, 63 (2016).
- [8] A. Bermudez, X. Xu, R. Nigmatullin, J. O’Gorman, V. Negnevitsky, P. Schindler, T. Monz, U. G. Poschinger, C. Hempel, J. Home, F. Schmidt-Kaler, M. Biercuk, R. Blatt, S. Benjamin, and M. Müller, Assessing the Progress of Trapped-Ion Processors Towards Fault-Tolerant Quantum Computation, *Phys. Rev. X* **7**, 041061 (2017).
- [9] T. Monz, D. Nigg, E. A. Martinez, M. F. Brandl, P. Schindler, R. Rines, S. X. Wang, I. L. Chuang, and R. Blatt, Realization of a scalable Shor algorithm, *Science* **351**, 1068 (2016).
- [10] P. Schindler, M. Müller, D. Nigg, J. T. Barreiro, E. Martinez, M. Hennrich, T. Monz, S. Diehl, P. Zoller, and R. Blatt, Quantum simulation of dynamical maps with trapped ions, *Nat. Phys.* **9**, 361 (2013).
- [11] R. Blatt and C. F. Roos, Quantum simulations with trapped ions, *Nat. Phys.* **8**, 277 (2012).
- [12] J. Zhang, G. Pagano, P. W. Hess, A. Kyprianidis, P. Becker, H. Kaplan, A. V. Gorshkov, Z.-X. Gong, and C. Monroe, Observation of a many-body dynamical phase transition with a 53-qubit quantum simulator, *Nature (London)* **551**, 601 (2017).
- [13] A. Steane, The ion trap quantum information processor, *Appl. Phys. B*, **64**, 623 (1997).
- [14] D. F. V. James, P. G. Kwiat, W. J. Munro, and A. G. White, Measurement of qubits, *Phys. Rev. A* **64**, 052312 (2001).
- [15] A. M. Hankin, E. R. Clements, Y. Huang, S. M. Brewer, J.-S. Chen, C. W. Chou, D. B. Hume, and D. R. Leibbrandt, Systematic uncertainty due to background-gas collisions in trapped-ion optical clocks, *Phys. Rev. A* **100**, 033419 (2019).
- [16] R. Blümel, J. Chen, E. Peik, W. Quint, W. Schleich, Y. Shen, and H. Walther, Phase transitions of stored laser-cooled ions, *Nature (London)* **334**, 309 (1988).
- [17] R. Blümel, C. Kappler, W. Quint, and H. Walther, Chaos and order of laser-cooled ions in a Paul trap, *Phys. Rev. A* **40**, 808 (1989).
- [18] M. Cetina, A. T. Grier, and V. Vuletić, Micromotion-Induced Limit to Atom-Ion Sympathetic Cooling in Paul Traps, *Phys. Rev. Lett.* **109**, 253201 (2012).
- [19] L. H. Nguyen, A. Kalev, M. D. Barrett, and B.-G. Englert, Micromotion in trapped atom-ion systems, *Phys. Rev. A* **85**, 052718 (2012).
- [20] Y. S. Nam, D. K. Weiss, and R. Blümel, Explicit, analytical radio-frequency heating formulas for spherically symmetric nonneutral plasmas in a Paul trap, *Phys. Lett. A* **381**, 3477 (2017).
- [21] V. L. Ryjkov, X. Zhao, and H. A. Schuessler, Simulations of the rf heating rates in a linear quadrupole ion trap, *Phys. Rev. A* **71**, 033414 (2005).
- [22] J. D. Tarnas, Y. S. Nam, and R. Blümel, Universal heating curve of damped Coulomb plasmas in a Paul trap, *Phys. Rev. A* **88**, 041401(R) (2013).
- [23] C. B. Zhang, D. Offenberg, B. Roth, M. A. Wilson, and S. Schiller, Molecular-dynamics simulations of cold single-species and multispecies ion ensembles in a linear Paul trap, *Phys. Rev. A* **76**, 012719 (2007).
- [24] R. Brewer, J. Hoffnagle, R. DeVoe, L. Reyna, and W. Henshaw, Collision-induced two-ion chaos, *Nature (London)* **344**, 305 (1990).
- [25] G. A. Gottwald and I. Melbourne, The 0-1 test for chaos: A review, in *Chaos Detection and Predictability* (Springer, Berlin, 2016), pp. 221–247.
- [26] M. Drewsen and A. Brøner, Harmonic linear Paul trap: Stability diagram and effective potentials, *Phys. Rev. A* **62**, 045401 (2000).
- [27] M. F. Brandl, M. W. van Mourik, L. Postler, A. Nolf, K. Lakhmanskiy, R. R. Paiva, S. Möller, N. Daniilidis, H. Häffner, V. Kaushal, T. Ruster, C. Warschburger, H. Kaufmann, U. G. Poschinger, F. Schmidt-Kaler, P. Schindler, T. Monz, and

- R. Blatt, Cryogenic setup for trapped ion quantum computing, *Rev. Sci. Instrum.* **87**, 113103 (2016).
- [28] J. D. Prestage, A. Williams, L. Maleki, M. J. Djomehri, and E. Harabetian, Dynamics of Charged Particles in a Paul Radio-Frequency Quadrupole Trap, *Phys. Rev. Lett.* **66**, 2964 (1991).
- [29] D. Freedman, R. Pisani, and R. Purves, *Statistics: Fourth International Student Edition* (Norton, New York, 2007).
- [30] L. Devroye, *Non-Uniform Random Variate Generation* (Springer-Verlag, New York, 1986).
- [31] C. Hempel, Digital quantum simulation, Schrödinger cat state spectroscopy and setting up a linear ion trap, Ph.D. thesis, University of Innsbruck, 2014.
- [32] R. Blatt, P. Zoller, G. Holzmüller, and I. Siemers, Brownian motion of a parametric oscillator: A model for ion confinement in radio frequency traps, *Z. Phys. D: At. Mol. Clusters* **4**, 121 (1986).
- [33] I. Siemers, R. Blatt, T. Sauter, and W. Neuhauser, Dynamics of ion clouds in Paul traps, *Phys. Rev. A* **38**, 5121 (1988).
- [34] M. Brownnutt, M. Kumph, P. Rabl, and R. Blatt, Ion-trap measurements of electric-field noise near surfaces, *Rev. Mod. Phys.* **87**, 1419 (2015).
- [35] D. J. Wineland and W. M. Itano, Laser cooling of atoms, *Phys. Rev. A* **20**, 1521 (1979).
- [36] L.-L. Yan, S.-I. Su, and M. Feng, Analytical investigation of one-dimensional Doppler cooling of trapped ions with λ -type configuration, *Phys. Rev. A* **100**, 033418 (2019).
- [37] H. J. Metcalf and P. van der Straten, Laser cooling and trapping of neutral atoms, in *The Optics Encyclopedia*, Vol. 38 (Wiley-VCH, Weinheim, Germany, 2007), pp. 847–853.
- [38] M. Hettrich, T. Ruster, H. Kaufmann, C. F. Roos, C. T. Schmiegelow, F. Schmidt-Kaler, and U. G. Poschinger, Measurement of Dipole Matrix Elements with a Single Trapped Ion, *Phys. Rev. Lett.* **115**, 143003 (2015).
- [39] F. Vedel, M. Vedel, and R. Evans March, New schemes for resonant ejection in r.f. quadrupolar ion traps, *Int. J. Mass Spectrom. Ion Processes* **99**, 125 (1990).
- [40] D. Kielpinski, C. Monroe, and D. J. Wineland, Architecture for a large-scale ion-trap quantum computer, *Nature (London)* **417**, 709 (2002).
- [41] J. B. Wübena, S. Amairi, O. Mandel, and P. O. Schmidt, Sympathetic cooling of mixed-species two-ion crystals for precision spectroscopy, *Phys. Rev. A* **85**, 043412 (2012).
- [42] C. Bruzewicz, R. McConnell, J. Stuart, J. Sage, and J. Chiaverini, Dual-species, multi-qubit logic primitives for Ca⁺/Sr⁺ trapped-ion crystals, *npj Quantum Inf.* **5**, 1 (2019).
- [43] C. C. Bradley, J. G. Story, J. J. Tollett, J. Chen, N. Ritchie, and R. G. Hulet, Laser cooling of lithium using relay chirp cooling, *Opt. Lett.* **17**, 349 (1992).
- [44] DOI: [10.5281/zenodo.5998292](https://doi.org/10.5281/zenodo.5998292).
- [45] DOI: [10.5281/zenodo.5884496](https://doi.org/10.5281/zenodo.5884496).